Empirical Constraints on the Nucleosynthesis of Nitrogen

James W. Johnson,[1][*] David H. Weinberg,[1,2,3] Fiorenzo Vincenzo,[1,2] Jonathan C. Bird,[4]
and Emily J. Griffith[1]

[1] *Department of Astronomy, The Ohio State University, 140 W. 18th Ave., Columbus, OH, 43210, USA*

[2] *Center for Cosmology and Astroparticle Physics (CCAPP), The Ohio State University, 191 W. Woodruff Ave., Columbus, OH, 43210, USA*

[3] *Institute for Advanced Study, 1 Einstein Dr., Princeton, NJ, 08540, USA*

[4] *Department of Physics & Astronomy, Vanderbilt University, 2301 Vanderbilt Place, Nashville, TN, 37235, USA*

ABSTRACT

We use a multi-ring galactic chemical evolution model to probe the astrophysical production of nitrogen (N) in the Milky Way. This approach treats individual annuli in the Galaxy disc as conventional one-zone models, and to include the effects of radial migration, stellar populations move between annuli in a manner based on star particles from a hydrodynamical simulation. We find that some recent AGB star yield tables are able to reproduce the gas-phase [N/O]-[O/H] relation as observed only if a substantial fraction of massive stars collapse to black holes. If instead most massive stars explode as supernovae, we must artificially increase N yields from AGB stars by factors of $2 - 3$ to offset the additional oxygen. We demonstrate that, with a viable set of AGB star yields, our model is able to reproduce many of the observed correlations between N, O, and Fe abundances for stars when the N abundances are corrected for internal mixing processes within stars. With any of these yields, N production timescales are sufficiently short such that stellar migration is only a minimal source of intrinsic scatter in the observed [N/O]-[O/H] relation. Modest variations in the star formation rate and star formation efficiency produce considerably larger variations in the gas phase N and O abundances, consistent with previous observational arguments. Our models run using the publicly available `Versatile Integrator for Chemical Evolution` (VICE; https://pypi.org/project/vice).

Key words: methods: numerical – galaxies: abundances, evolution, star formation, stellar content

1 INTRODUCTION

• In terms of astrophysical nucleosynthesis, nitrogen (N) is a unique element.

– It's one of only a few elements lighter than strontium (Z = 38) with significant nucleosynthetic yields from asymptotic giant branch (AGB) stars (Johnson 2019).

– Alongside helium, it is one of the primary nuclear fusion products of main sequence stars more massive than the sun with nonzero metallicity. The CNO cycle[1] catalyses the proton-proton chain of nuclear reactions (e.g. Suliga, Shalgar & Fuller 2020) using carbon (C), N, and oxygen (O) target nuclei, the slowest component of which is the ^{14}N(p,γ)^{15}O reaction. This bottleneck is a sufficiently strong effect such that, to first order, the effect of the CNO cycle is to convert all of the C and O isotopes in a star into ^{14}N.

– It's among a select group of elements whose observed abundances in stellar spectra often do not reflect the star's birth abundances. Internal mixing processes (particularly dredge-up) changes the surface abundances of C and N in red giants, a phenomenon both expected from theoretical models and observed in open and globular clusters (Gilroy 1989; Korn et al. 2007; Lind et al. 2008; Souto et al. 2018, 2019).

• Both observationally and theoretically, N is among the more well studied elements. Fig. 1 presents a compilation of observed abundances of N and O in the gas phase:

– HII regions in the first six CHAOS galaxies (NGC 3184, NGC 628, NGC 5194, NGC 5457, M101, and NGC 2403; Berg et al. 2020; Skillman et al. 2020; Rogers et al. 2021).
– HII regions in nearby NGC spirals (Pilyugin et al. 2010)
– HII regions in blue, diffuse star forming dwarf galaxies (Berg et al. 2012; Izotov et al. 2012; James et al. 2015)
– Local stars and HII regions (Dopita et al. 2016)
– Galactic and extragalactic HII regions (Henry et al. 2000)
– Star-forming regions in 550 nearby galaxies in the MaNGA IFU survey (Belfiore et al. 2017)

Despite intrinsic scatter and some systematic variation in how the abundances are determined, the [N/O]-[O/H][2] relation is more or less the same across a wide range of physical enrivonments.

• In this paper, we're interested in the origin of both the shape and scatter in this trend.

---

[*] Contanct e-mail: johnson.7419@osu.edu
[1] ^{12}C(p,γ)^{13}N(β^+,ν_e)^{13}C(p,γ)^{14}N(p,γ)^{15}O(β^+,ν_e)^{15}N(p,α)^{12}C

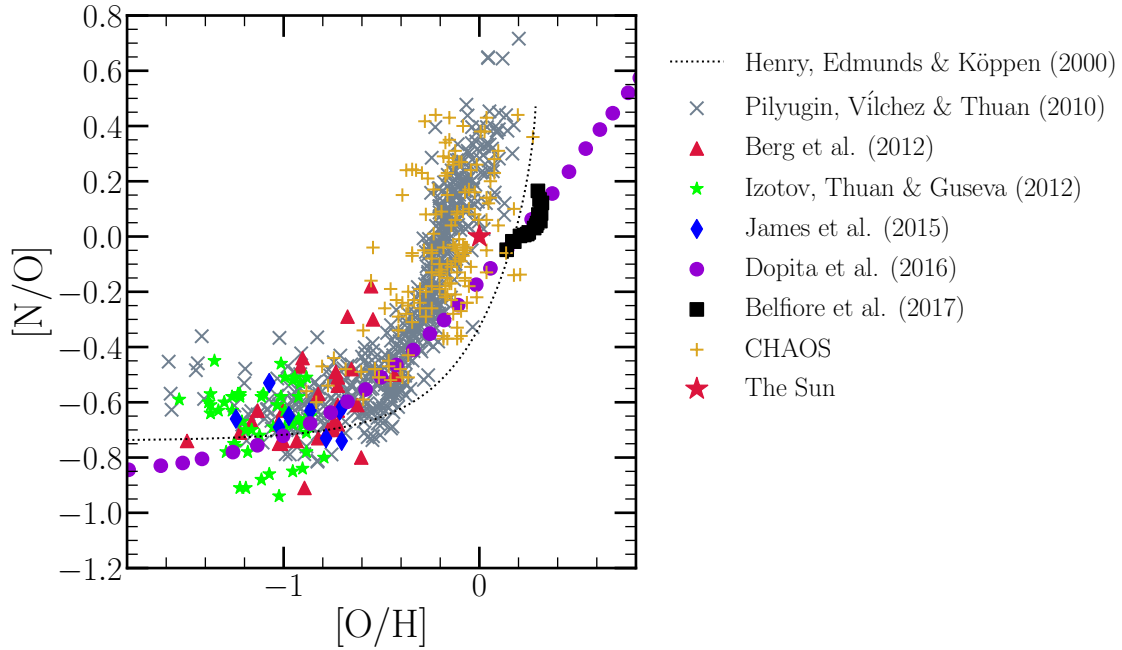[2] We follow the standard notation where [X/Y] $\equiv$ $\log_{10}(X/Y)$ − $\log_{10}(X/Y)_\odot$.

Figure 1. The [N/O]-[O/H] relation as observed in different galactic environments: HII regions from the first six CHAOS galaxies (golden +'s: NGC 3184, NGC 628, NGC 5194, NGC 5457, M101, and NGC 2403; Berg et al. 2020; Skillman et al. 2020; Rogers et al. 2021) and other nearby NGC spiral galaxies (grey X's: Pilyugin, Vílchez & Thuan 2010), HII regions in blue, diffuse star forming dwarf galaxies (red triangles: Berg et al. 2012; green stars: Izotov, Thuan & Guseva 2012; blue diamonds: James et al. 2015), in local stars and HII regions (purple circles: Dopita et al. 2016), and in the MaNGA IFU survey (black squares: Belfiore et al. 2017). The fit to [N/O] as a function of [O/H] in Galactic and extragalactic HII regions by Henry, Edmunds & Köppen (2000) is shown in a black dotted line. The Sun, at (0, 0) on this plot by definition, is marked by a red star. We omit the uncertainties for visual clarity. To do: Pull the data Noah Rogers's paper on NGC 2403 and add it to this figure.

• N is not unique in that perhaps the largest source of uncertainty in modeling its abundances is that accurate and precise nucleosynthetic yields remain elusive.

– Presently, no combination of core collapse supernova explosion model and black hole landscape has been able to reproduce the observed abundance pattern of the elements, and nitrogen is no exception (Griffith et al. 2021). Recently, Grisoni, Matteucci & Romano (2021) argued that rotating massive stars play a key role in establishing the N abundances seen in metal-poor stars in the Milky Way. Rotation has a considerable impact on the N yields of massive stars, particularly at low metallicity, because the internal mixing that it causes (Zahn 1992; Maeder & Zahn 1998; Lagarde et al. 2012) brings internally produced C and O nuclei into the hydrogen burning shell where they can be processed into ^{14}N via the CNO cycle (Heger & Woosley 2010; Frischknecht et al. 2016; Andrews et al. 2017). We find similar results here comparing theoretical models of CCSN nucleosynthesis (see discussion in § 2.1).

– Theoretical models of AGB star nucleosynthesis predict N yields to vary as a function of both progenitor mass and metallicity (Cristallo et al. 2011, 2015; Karakas 2010; Karakas & Lugaro 2016; Karakas et al. 2018; Ventura et al. 2013). In sufficiently massive AGB stars, the base of the convective envelope is hot enough to activate proton capture reactions, allowing the CNO cycle to convert C and O isotopes into ^{14}N: a process known as hot bottom burning (HBB). If the AGB star is also experiencing thermal pulsations, then with each pulse the convective envelope penetrates into the CO-rich core and brings some of this material into the hydrogen burning region: a process known as third dredge-up (TDU). When both processes are active, each TDU episode adds

new seed nuclei for HBB to turn into ^{14}N, substantially increasing N yields. We demonstrate in §§ 2.2 and 2.3 that various theoretical models predict significantly different N yields for high mass AGB stars as a consequence of how TDU and HBB occur in the models. The differences in these processes are in turn a consequence of the microphysical assumptions built into the stellar evolution models (e.g. mass loss, convection and convective boundaries, nuclear reaction networks).

• In this paper, we aim to constrain N yields from AGB stars empirically by assessing their ability to reproduce the observed abundance correlations between N and O, such as that illustrated in Fig. 1. Vincenzo et al. (2021) demonstrate that when N abundances are corrected for internal mixing processes, the correlations with stellar age and other elemental abundances are affected; whether or not these correlations can be reproduced in galactic chemical evolution (GCE) models is also of central interest to this paper.

• In a sample of 6,507 galaxies from the Mapping Galaxies at Apache Point Observatory survey (MaNGA; Bundy et al. 2015), Schaefer et al. (2020) recently argued that intrinsic scatter in the [N/O]-[O/H] relation is a consequence of variations in the local star formation efficiency. In regions of slower star formation, the [N/O] ratio tends to be slightly higher at fixed [O/H] (see their Fig. 4), as expected from GCE models (e.g. Mollá et al. 2006; Vincenzo et al. 2016a). However, Schaefer et al. (2020) could not rule out radial migration as an additional source of scatter in the gas phase [N/O]-[O/H] relation. Investigating GCE models for O and iron (Fe) abundances in the Milky Way which track the positions of stars as they migrate within the disc, Johnson et al. (2021) found that the characteristic delay time of type Ia supernovae (SNe Ia) is suffi-

ciently long such that stellar migration has a noticeable impact on the Fe abundance in the ISM at a given Galactocentric radius and time. Since N is produced in significant quantities by AGB stars, which like SNe Ia are delayed nucleosynthetic sources, it's possible that its gas phase abundance could be affected by a deficit or surplus of AGB stars induced by radial migration; in a sufficiently large sample of galaxies like MaNGA this would present observationally as scatter in the gas phase abundances. The question of whether one of radial migration or star formation efficiency dominates over the other in driving this scatter is also of central interest in this paper.

2 NUCLEOSYNTHESIS

• Although we're computing abundances for N, O, and Fe in the present paper, O and Fe were already explored in detail by Johnson et al. (2021), and we retain their parameterization of O and Fe supernova yields here. As required by VICE, the supernova yields are defined as the net mass of some element X produced over all explosion events in units of the progenitor star cluster's mass. For example, with a yield of $y_X = 0.001$, a 1000 $M_\odot$ cluster would produce 1 $M_\odot$ of the element X instantaneously in the case of CCSNe or over the delay time distribution (DTD) in the case of SNe Ia. We take the following values from Johnson et al. (2021), who in turn base them off of Weinberg et al. (2017) and Johnson & Weinberg (2020):

- $y_O^{CC} = 0.015$
- $y_{Fe}^{CC} = 0.0012$
- $y_O^{Ia} = 0$
- $y_{Fe}^{Ia} = 0.00214$

• We set y_N^{Ia} to zero and spend the remainder of this section detailing our CCSN and AGB star yields of N.

2.1 Core Collapse Supernovae and Massive Star Winds

• In VICE, CCSN nucleosynthetic products are approximated to be produced instantaneously following an episode of star formation; this is a valid approximation due to how short the lives of massive stars are compared to the relevant timescales for GCE. The yield is the constant of proportionality between the CCSN production rate and the SFR:

$$\dot{M}_X^{CC} = y_X^{CC} \dot{M}_\star. \qquad (1)$$

More generally, y_X^{CC} quantifies *all* of the nucleosynthetic material approximated to be produced instantaneously following a single stellar population's formation, though the majority of such events will be associated with massive stars and their supernovae. In the case of N specifically, a substantial amount emerges in winds before the actual supernova explosion itself, allowing massive stars to produce a lot of N even if they collapse directly to a black hole (Griffith et al. 2021).

• We compute theoretically predicted values of y_N^{CC} assuming a Kroupa (2001) IMF using VICE's `vice.yields.ccsne.fractional` function; details on how VICE handles these calculations can be found in § 4 of Griffith et al. (2021) and in the VICE science documentation.[1] The left panel of Fig. 2 plots the results as a function of progenitor

[1]   https://vice-astro.readthedocs.io/en/latest/science_documentation/yields/index.html

metallicity predicted by the Woosley & Weaver (1995), Nomoto et al. (2013), Sukhbold et al. (2016), and Limongi & Chieffi (2018) tables.

• There is good agreement between the various non-rotating models, but only Limongi & Chieffi (2018) report yields for progenitors with a non-zero rotational velocity. These yields are substantially larger than that of their non-rotating counterparts. Most of the N production in CCSN progenitors occurs via the CNO cycle processing C and O isotopes into ^{14}N, and with few C and O seed nuclei at low Z, production of ^{14}N is difficult. Rotationally induced mixing, a highly uncertain process (Zahn 1992; Maeder & Zahn 1998; Lagarde et al. 2012), could transport newly produced C and O into the hydrogen burning shell of the CCSN progenitor, facilitating N production (Frischknecht et al. 2016; see also discussion in § 4.2 of Andrews et al. 2017). For this reason, N yields at low metallicity are quite sensitive to these assumptions about stellar rotation and internal mixing processes (Heger & Woosley 2010), and consequently IMF-averaged yields are highly uncertain.

• Based on the definition of the abundance ratio [X/Y], we can compute the [N/O] ratio of CCSN ejecta from the values of y_N^{CC} and y_O^{CC}:

$$[N/O]_{cc} = \log_{10}\left(\frac{y_N^{CC}}{y_O^{CC}}\right) - \log_{10}\left(\frac{Z_{N,\odot}}{Z_{O,\odot}}\right) \qquad (2)$$

where $Z_{X,\odot}$ is the abundance by mass of some element X in the sun. For each of the studies and rotational velocities in the left panel of Fig. 2, we compute the corresponding values of y_O^{CC} using VICE, and we plot the resultant values of [N/O]$_{cc}$ in the right panel assuming $Z_{N,\odot} = 6.91 \times 10^{-4}$ and $Z_{O,\odot} = 5.7 \times 10^{-3}$ based on the solar photospheric abundances of Asplund et al. (2009). The resultant values of [N/O]$_{cc}$ follow similar trends with progenitor metallicity and rotational velocity as y_N^{CC}, a consequence of the fact that these studies predict relatively metallicity-independent O yields.

• At low [O/H], the mean [N/O] is near −0.7 (see Fig. 1). Since the AGB star yields of N are believed to increase with metallicity (e.g. Cristallo et al. 2011, 2015; Ventura et al. 2013), this is likely the regime in which N yields are dominated by CCSN enrichment. We therefore take [N/O]$_{cc}$ = −0.7 empirically, and we highlight this value in the right panel of Fig. 2 with a horizontal black dashed line. Given this result, we use equation (2) with our adopted value of $y_O^{CC} = 0.015$ and the solar abundances from Asplund et al. (2009) to compute an empirical value of $y_N^{CC} = 3.6 \times 10^{-4}$. We adopt this value as our fiducial CCSN yield of N and highlight it with a horizontal black dashed line in the left hand panel of Fig. 2. We discuss the sloped dotted line in that panel in the context of some of our AGB star yield models in § 4.2.

• These empirical values of [N/O]$_{cc}$ and y_N^{CC} are in good agreement with the rotating CCSN models of Limongi & Chieffi (2018). This supports the recent argument by Grisoni, Matteucci & Romano (2021) that rotating massive stars play an important role in establishing the N abundances observed at low metallicities in the Milky Way. Although the Sukhbold et al. (2016) tables agree nearly perfectly with our empirical value of $y_N^{CC} = 3.6 \times 10^{-4}$, they overestimate [N/O]$_{cc}$ by ~0.2 dex; this is because they predict a value of y_O^{CC} lower than our adopted value of 0.015.

• Although most of the supernova models plotted in Fig. 2 slightly overestimate our empirical value of [N/O]$_{cc}$ = −0.07, they're still subsolar. This implies a need for an additional enrichment channel, as expected because it is well-understood that N is also produced in AGB stars (Johnson 2019).
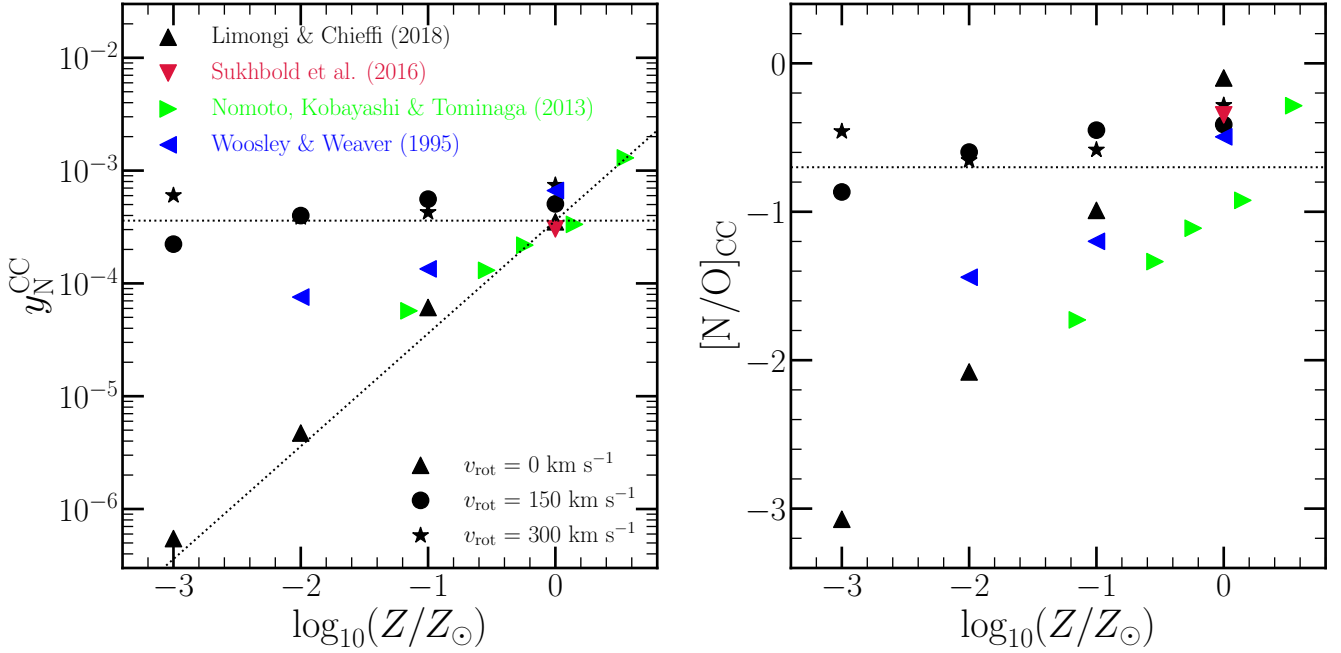
Figure 2. **Left**: IMF-averaged CCSN yields of N calculated using VICE's `vice.yields.ccsne.fractional` function with the tables published by Woosley & Weaver (1995, blue), Nomoto, Kobayashi & Tominaga (2013, green), Sukhbold et al. (2016, red), and Limongi & Chieffi (2018, black). All studies report yields for non-rotating progenitors, shown by the triangles; for visual clarity, the triangles point in a different direction for each study according to the legend. Limongi & Chieffi (2018) report additional yields for progenitors with rotational velocities of 150 (circles) and 300 km/s (stars). The horizontal dotted line marks $y_N^{CC} = 3.6 \times 10^{-4}$, the value of our fiducial CCSN yield of N in our GCE models. We use the form shown by the slanted line (equation 6) in § 4.2 in combination with some of our AGB star yield models discussed in § 2.2. **Right**: The [N/O] ratio predicted by each of the explosion models in the left-hand panel, under the same colour-coding and marker scheme. We mark the position of [N/O] = −0.7 with a black dotted line, the value roughly suggested by the observations of low-metallicity systems highlighted in Fig. 1.

2.2 Asymptotic Giant Branch Stars

• In the present paper, we're interested in the question of how well the "off the shelf" AGB star yield models for N can reproduce the observed [N/O]-[O/H] relation.

• Similar to the SN yields (see discussion above), these are defined as fractional net yields in that they quantify only the newly produced N in the AGB star ejecta in units of its ZAMS mass. For a yield $y_N^{AGB}(M_\star, Z_\star)$, the actual mass yield is then given by $M_\star y_N^{AGB}(M_\star, Z_\star)$. AGB star enrichment proceeds as it does in Johnson & Weinberg (2020) under the caveat that the yield is placed in the $\delta R_{gal} = 100$ pc ring that a stellar population is in at a given time. In short, VICE implements an algorithm which calculates the mass in dying stars from each previous star formation event (i.e. timestep), and the ZAMS mass required to calculate the yield comes from a mass-lifetime relation (e.g. Larson 1974; Maeder & Meynet 1989; Padovani & Matteucci 1993; Kodama & Arimoto 1997; Hurley, Pols & Tout 2000; Vincenzo et al. 2016b).

• In the present paper, we make use of four previously published sets of AGB star yields calculated from stellar evolution models, each of which are sampled on a table of progenitor masses and metallicities:

– The default set of yields is published in Cristallo et al. (2011, 2015, hereafter C11+C15). We illustrate these yields as a function of ZAMS mass for the available metallicities in the lower left panel of Fig. 3. This is the most comprehensive set of yields in VICE in that it includes tables for all elements built into the code and is sampled at the most metallicities.

– The Karakas (2010, hereafter K10) is plotted in the upper left panel of Fig. 3.

– We combine the yields published in Karakas & Lugaro (2016) at $Z = 0.007$, 0.014, and 0.03 with those published in Karakas et al. (2018) at $Z = 0.0028$; we hereafter refer to these tables as the KL16+K18 set of yields. We plot them in the upper middle panel of Fig. 3.

– We combine the yields for $Z = 0.0003$ and $Z = 0.008$ progenitors from Ventura et al. (2013) with those at $Z = 0.004$ from Ventura et al. (2014), at $Z = 0.014$ from Ventura et al. (2018), and at $Z = 0.04$ from Ventura et al. (2020) into a single table of yields. We also include a set of un-published yields at $Z = 0.001$ and $Z = 0.002$ (provided by P. Ventura, private communication). We hereafter refer to this model as the V13 yield set, and we illustrate it in the top right panel of Fig. 3.

• VICE also allows users to construct their own functions of progenitor mass and metallicity to describe the AGB star yield. Motivated by the roughly linear nature of the C11+C15 yields and their general success once renormalized by a constant factor (see discussion in § 4), we construct a model in which the yield is linearly proportional to both progenitor ZAMS mass and metallicity according to:

$$y_N^{AGB} = \xi \left(\frac{M}{M_\odot} \right) \left(\frac{Z}{Z_\odot} \right) \tag{3}$$

We illustrate this model in the lower right panel of Fig. 3 for $\xi = 3 \times 10^{-4}$ in comparison to the C11+C15 yields shown by the coloured X's.
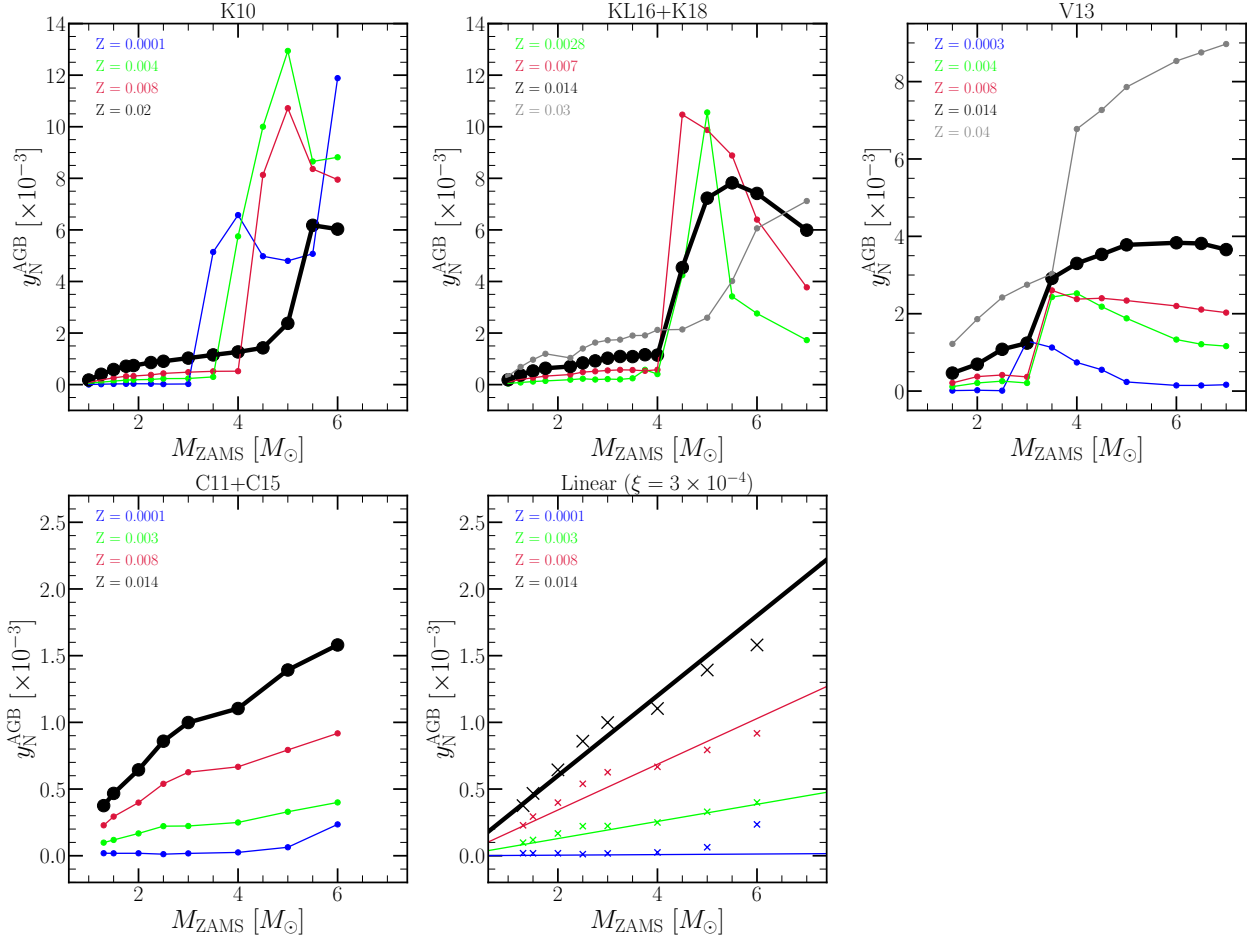
Figure 3. The fractional yields of N from AGB stars y_N^{AGB} as a function of progenitor ZAMS mass and birth metallicity Z as reported by Karakas (2010) (upper left), Karakas & Lugaro (2016) and Karakas et al. (2018) (upper middle), Ventura et al. (2013) (upper right), and Cristallo et al. (2011, 2015) (lower left). For Ventura et al. (2013) and Cristallo et al. (2011, 2015), we show the yields for a selection of metallicities available from their provided tables. The yields at solar metallicity ($Z = 0.02$ for Karakas 2010, $Z = 0.014$ otherwise) are highlighted by a thick black line. In the lower right panel, we show the yields predicted by our linear model (coloured lines; see discussion in § 2.2) in comparison to the Cristallo et al. (2011, 2015) predictions (coloured X's).

• Despite reporting values of the same physical quantities, the N yields reported by each of these studies show substantial differences between one another. Unfortunately, ascertaining the origins of these differences is difficult because each study employs different assumptions for mass loss, nuclear reaction networks, and convection and convective boundaries within the star, all of which have a significant impact on stellar evolution and thus the predicted yields (see discussion in, e.g., § 5 of Karakas & Lugaro 2016). However, the differences can largely be understood by considering two phenomena known to occur within AGB stars: third dredge-up and hot bottom burning. Collapsing the information into these two processes is helpful because their differences arise as a consequence of the different input physics between the stellar evolution models.

    – Third dredge-up (hereafter TDU)[2] refers to the repeated penetrations of the convective envelope into the hydrogen depleted

core during the thermal pulses associated with AGB star evolution. This process doesn't affect N abundances much, but replenishes the outer layers of the star with C and O. In low mass AGB stars, the main source of free neutrons is the $^{13}C(\alpha,n)^{16}O$ reaction, which can occur at substantial rates when C is mixed with the He-rich shell during each TDU episode.

    – Hot bottom burning (hereafter HBB) refers to the activation of proton captures at the base of the convective envelope activating the CNO cycle and producing large amounts of ^{14}N at the expense of C and O isotopes. HBB requires a higher mass AGB star progenitor ($\sim$4 - 5 $M_\odot$ at $Z_\odot$) than TDU ($\sim$2 - 2.5 $M_\odot$ at $Z_\odot$), but the minimum mass for both decreases at lower metallicity.

• The most efficient N production occurs when both TDU and HBB occur within an AGB star, because each replenishment of C and O isotopes from the core adds new seed nuclei for the CNO cycle when HBB is active. This is the reason for the substantial N production above $\sim$4 $M_\odot$ in the K10 and KL16+K18 models; in both yield sets, every star that experiences HBB also experiences TDU. Both TDU and HBB are more efficient at low metallicity (see discussion in V13). In the case of TDU, each penetration of the convective envelope into the H-depleted core is deeper because of the lower opacity. For HBB, the base of the convective envelope is

---

[2] Here the time adverbial "third" refers only the fact that the star is on the asymptotic giant branch. First dredge-up occurs when a star first ascends the red giant branch, and second dredge-up occurs when the star ends its helium-burning lifetime. Because TDU episodes are associated with thermal pulsations, there are many TDU events during a star's AGB lifetime.

hotter, increasing the rate of nuclear reactions relative to the higher Z models. Though there are some exceptions evident in Fig. 3, the highest N yields in the K10 and KL16+K18 models are for low metallicity stars above ~4 $M_\odot$ for exactly this reason.

• This interaction between TDU and HBB is also the reason for the increase in N yields in the V13 tables near ~3 $M_\odot$. Unlike the K10 and KL16+K18 models, their stars experience both TDU and HBB only in this narrow range in mass.

• Of all of these yields taken from the literature, the C11+C15 sample shows the smoothest dependence on progenitor mass and metallicity. Unfortunately, ascertaining the exact cause of this difference between the other yields explored here is difficult even when collapsing the information into TDU and HBB; relative to the KL16+K18 yields (see discussion in their § 5), the C11+C15 models have more mass loss, a ~10% faster triple-α reaction rate, fewer thermal pulses overall, and weaker HBB due to a lower temperature at the base of the convective envelope. Though their agreement is good below ~3 $M_\odot$, the fact that HBB is weaker and fewer TDU episodes are experienced does however lend a qualitative explanation into why the C11+C15 yields are so much smaller than the K10 and KL16+K18 yields at higher masses.

• Although both the KL16+K18 and K10 yield models show a considerable increase in N yields above ~ $4M_\odot$, there are some notable differences between the two.

– In particular, the yields at solar metallicity ($Z = 0.014$ in the KL16+K18 models, but $Z = 0.02$ in K10) are somewhat higher in the newer version. Although some of this can be attributed to the now-lowered solar metallicity, it does not account for the entirety of the effect. Furthermore, the yields at sub-solar metallicities decreased slightly, particularly for the highest mass stars in these models.

– These differences can be understood by slight variations in the input physics (A. Karakas, private communication). Based on updated opacity tables, the newer models are slightly hotter and more compact; as a consequence, they experience hotter HBB and deeper TDU. Experiencing more thermal pulses overall and consequently a longer AGB lifetime, the KL16+K18 stars have more time for HBB to convert ^{12}C into ^{14}N. At lower metallicity, KL16+K18 use low-temperature opacities based on Marigo (2002) that follow the surface composition of the star. These opacities are higher, making the stars larger and increasing the mass-loss rate. The $Z = 0.0028$ model from Karakas et al. (2018) uses the Bloecker (1995) mass-loss prescription as opposed to that of Vassiliadis & Wood (1993) as in both Karakas (2010) and Karakas & Lugaro (2016). This choice results in fewer thermal pulses and a shorter AGB lifetime. Each of these effects at low metallicity act to decrease the overall yield of ^{14}N.

• In the interest of consistency, when we adopt a particular AGB star yield model for N, we also adopt it for O and Fe when possible.[3] However, the AGB star yields of these elements are negligible compared to their supernova yields.

2.3 IMF-Averaged AGB Yields: Metallicity and Time Dependence

• To more directly compare these AGB star yield tables to one another, in the right hand panel of Fig. 4 we plot the IMF-weighted mass yields of N reported by the C11+C15, V13, K10,

and KL16+K18 models at solar metallicity (i.e. $Z = 0.02$ for K10, $Z = 0.014$ otherwise).

– As mentioned in § 2.2, the AGB star yield of N y_N^{AGB} is in units of the progenitor star's ZAMS mass, and consequently the *mass yield* of N is given by $M_\star y_N^{AGB}$. With an additional weight of $M_\star^{-2.3}$ from the IMF in this mass range (Kroupa 2001), we therefore multiply the values of y_N^{AGB} by $(M_\star/M_\odot)^{-1.3}$ to quantify the total mass yield of N taking into account the intrinsic mass distribution of stars.

– Even with the additional weighting of $M_\star^{-1.3}$, the C11+C15 yields are relatively mass-independent. Because of the steep nature of the stellar mass-lifetime relation (e.g. Larson 1974; Maeder & Meynet 1989; Padovani & Matteucci 1993; Hurley et al. 2000), the N produced by single stellar populations is still dominated by higher mass ($\gtrsim 2M_\odot$) AGB stars; in other words, the enrichment rates will inevitably slow down considerably for old stellar populations once the mass of its AGB stars depends only weakly on age. For other studies, the contributions from higher mass AGB stars is yet more pronounced due to the effects of TDU and HBB discussed in § 2.2. For these yield models, the characteristic delay times of N will be even shorter due to the enhanced contributions of shorter-lifetime stars.

• In the middle panel of Fig. 4, we plot the fractional AGB star production of N as a function of stellar population age.

– We use VICE's `vice.single_stellar_population` function, which computes the mass yield of a given element as a function of age from a star cluster of known metallicity. For the sake of this calculation, we set y_N^{CC} to zero in order to highlight the AGB star production. We show the results of this procedure for solar metallicity only ($Z = 0.02$ for K10, $Z = 0.014$ otherwise), and we normalize by the total mass produced at $T = 13.2$ Gyr.

– Under the C11+C15 yields, it takes ~250 Myr for a single stellar population to produce ~50% of its N from AGB stars, as noted by the colored points at the top of the panel. The alternate yield models, with larger contributions from higher mass AGB stars, have shorter characteristic delay times.

– For comparison, we plot the enrichment of Fe by our $t^{-1.1}$ power-law DTD, also with the CCSN yield set to zero to highlight the SN Ia contribution. The characteristic delay time for Fe production is longer than that of N by nearly an order of magnitude, and by exactly how much depends slightly on which AGB star yield model is selected. As noted in Johnson et al. (2021), a delay-time of ~1 Gyr is exactly as expected for a ~ t^{-1} DTD because half of the SNe Ia occur between 100 Myr and 1 Gyr and the other half between 1 and 10 Gyr.

• In the right panel of Fig. 4, we plot the total amount of N produced by a 13.2 Gyr old single stellar population as a function of its metallicity according to all four of the AGB star yield models; we have normalized these values by the initial mass of the stellar population.

– In general, there is good qualitative agreement between the C11+C15 and the V13 models, the only major difference being the normalization. Up to $\log_{10}(Z/Z_\odot) \approx -0.2$, the KL16+K18 yields predict a similar trend as C11+C15 and V13, also with a difference in normalization, but at higher metallicities the predict N yields are much more metallicity-independent than others. The K10 yields, on the other hand, do not agree with any of the others. Instead, they predict the N yields to *decrease* monotonically with increaasing Z. The predictions with the linear

---

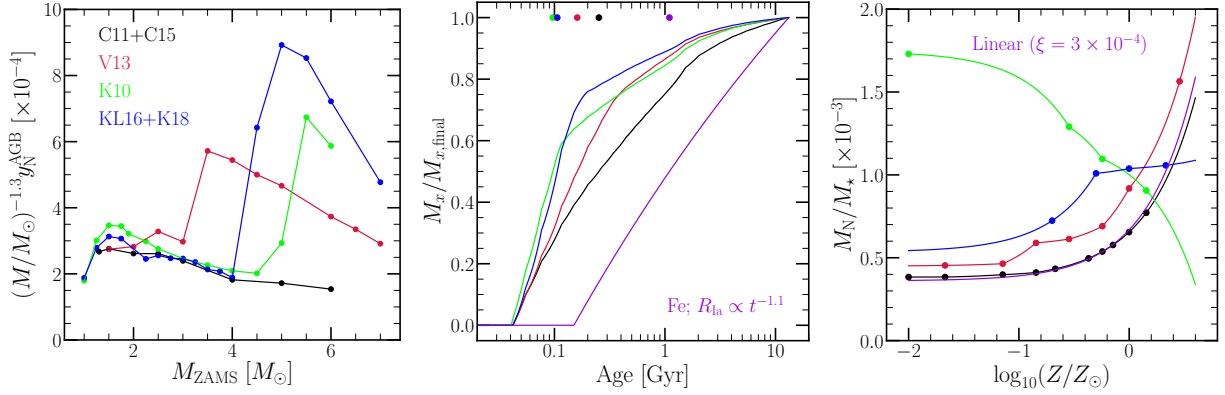[3] In the case of the V13 model, AGB star yields of Fe are not available.

Figure 4. **Left**: The IMF-weighted mass yield of N from AGB stars as a function of progenitor mass at solar metallicity ($Z = 0.02$ in K10, $Z = 0.014$ otherwise). **Middle**: The net mass of N produced by AGB stars from a single stellar population for each of our yield models at the same metallicities as in the left panel. The purple line denotes the same for Fe assuming our $t^{-1.1}$ delay time distribution. All values are normalized to the total mass produced at an age of 13.2 Gyr. Points at the top of the panel denote the ages at which 50% of the total mass yield has been produced. **Right**: The total amount of N produced by a 13.2 Gyr old stellar population as a function of metallicity for each of our yield models normalized by the stellar population's initial mass. Points mark metallicities at which the published tables report yields.

model are nearly identical to the C11+C15 model, though this is unsurprising given their similarity in Fig. 3.

3 THE MULTI-ZONE CHEMICAL EVOLUTION MODEL

- Since we wish to test the impact of various assumptions about nucleosynthetic yields while taking into account stellar migration, multi-zone chemical evolution models are the ideal experiments. This allows us not only to entertain different assumptions regarding nucleosynthetic yields of N, but also affords us the ability to enforce a specific star formation history as well as slight variations to any of these assumptions - all within a framework that includes the impact of radial migration.

- We make use of the Milky Way models of Johnson et al. (2021), who originally constructed the model to explore the impact of stellar migration on the observed abundances of O and Fe. This model makes use of the Versatile Integrator for Chemical Evolution (VICE; Johnson & Weinberg 2020; Griffith et al. 2021; Johnson et al. 2021), an open-source python package for Unix system architectures. Because VICE recognizes most elements on the periodic table, computing N abundances with this model is easy. Though we provide a brief summary here, a full breakdown of the Johnson et al. (2021) model can be found in their § 2.

- As in previous models for the Milky Way (e.g. Matteucci & Francois 1989; Schönrich & Binney 2009; Minchev et al. 2013, 2014, 2017; Sharma et al. 2020), this model parameterizes the Galaxy disc as a series of concentric rings of width $\delta R_{\rm gal} = 100$ pc. Each ring is assigned its own star formation history (SFH), and with assumptions about the $\Sigma_{\rm gas} - \dot{\Sigma}_\star$ relation and outflows (see discussion below), VICE calculates the implied amounts of gas and infall at each timestep automatically. Each ring is assumed to be described by a conventional one-zone model of chemical evolution under the caveat that stellar populations can move between rings, which Johnson et al. (2021) demonstrate has a significant impact on the enrichment rates of delayed sources such as SNe Ia.

- To drive stellar migration, the model makes use of star particles from a hydrodynamical simulation, for which Johnson et al. (2021) chose the h277 galaxy from the Christensen et al. (2012) suite evolved

with the N-body+SPH code GASOLINE (Wadsley et al. 2004); we retain this decision here. Previous studies have shown that h277, among other disc galaxies evolved with similar physics, has a realistic rotation curve (Governato et al. 2012; Christensen et al. 2014a,b), stellar mass (Munshi et al. 2013), metallicity (Christensen et al. 2016), dwarf satellite population (Zolotov et al. 2012; Brooks & Zolotov 2014), HI properties (Brooks et al. 2017), and age-velocity relation (Bird et al. 2021).

- Despite this, there are some interesting differences between h277 and the Milky Way. The last major merger in h277 was at a redshift of $z \approx 3$, making it an interesting case study for its quiescent merger history (e.g. Zolotov et al. 2012). The Milky Way is also known to have a strong, long-lived bar (e.g. Bovy et al. 2019), while h277 had only a weak and transient bar, lacking one at the present day.

- Radial migration proceeds from the h277 star particles in a simple manner; for a stellar population in our model born at a radius $R_{\rm gal}$ and a time T, VICE searches for star particles born at $R_{\rm gal} \pm$ 250 pc and $T \pm 250$ Myr. From the star particles that pass this cut, it then randomly selects one to act as that stellar population's *analogue*. The stellar population then assumes the present day midplane distance z and the change in orbital radius $\Delta R_{\rm gal}$ of its analogue. In the Johnson et al. (2021) fiducial model, stellar populations move to their implied final radii with a $\sqrt{\rm age}$ dependence, similar to the assumption made by Frankel et al. (2018, 2019). While they investigate the impact of this assumption, in the present paper we make use of only this model and one in which stellar migration is ignored. If VICE does not find any star particles from h277 in its initial search, it widens it to $R_{\rm gal} \pm 500$ pc and $T \pm 500$ Myr; if still no candidate analogues are found, VICE maintains the $T \pm 500$ Myr requirement, but assigns the star particle with the smallest difference in birth radius as the analogue. As in Johnson et al. (2021), these models neglect the impact of radial gas flows (e.g. Lacey & Fall 1985; Bilitewski & Schönrich 2012; Vincenzo & Kobayashi 2020), instead focusing on the impact of stellar migration.

- Although this model does impose some small but nonzero level of star formation at early times in the outer disc, the sample of star particles from h277 is sufficiently large that stellar populations that form there are typically assigned analogues which formed within ~2 kpc of their birth radius. While ignoring effects such as the radial

growth of the Galaxy (e.g. Bird, Kazantzidis & Weinberg 2012; Bird et al. 2013), this at least ensures that these old, outer disc populations are assigned stellar populations which give them an outer disc rather than an inner disc dynamical history.

• Rather than using a hydrodynamical simulation, some previous studies have implemented stellar migration using dynamical arguments (e.g. Schönrich & Binney 2009; Sharma et al. 2020).

– An advantage of our approach over this is that these dynamical arguments introduce free parameters into the model which then require fitting to data. A disadvantage is that we are restricted to one realization of our dynamical history; slight variations are not possible.

– This model does not distinguish between "blurring" and "churning", terms often used to refer to a the epicyclic motions of stars and changes in their guiding centres, respectively. These effects are induced by a variety of physical interactions such as molecular cloud scattering (Mihalas & Binney 1981; Jenkins & Binney 1990; Jenkins 1992), orbital resonances with spiral arms or bars (Sellwood & Binney 2002; Minchev et al. 2011), and satellite perturbations (Bird et al. 2012); both are present in h277.

• Our fiducial model here has the same SFH as that of Johnson et al. (2021), where the time-dependence at a given R_{gal} is given by:

$$\dot{\Sigma}_\star(t|R_{gal}) \propto (1 - e^{-t/\tau_{rise}})e^{-t/\tau_{sfh}}, \quad (4)$$

where τ_{rise} approximately controls the amount of time the SFR is rising at early times; we set this parameter equal to 2 Gyr at all radii as in Johnson et al. (2021). Our e-folding timescales τ_{sfh} are taken from a fit of this functional form to the $\Sigma_\star$-age relation in bins of R/R_e for $10^{10.5} - 10^{11}$ M$_\odot$ Sa/Sb Hubble type spiral galaxies reported by Sánchez (2020). The resulting values of τ_{sfh} are long: ∼15 Gyr at the solar circle ($R_{gal} = 8$ kpc) and as high as ∼40 Gyr in the outer disc (see their Fig. 3), which is primarily a consequence of the flat nature of the $\Sigma_\star$-age relation reported by Sánchez (2020).

• Within each $\delta R_{gal} = 100$ pc ring, the normalization of the SFH is set by the total stellar mass of the Milky Way disc and the present-day surface density gradient assuming it is unaffected by stellar migration (see Appendix B of Johnson et al. 2021). For the former, we neglect the contribution from the bulge and adopt the total disc stellar mass of 5.17×10^{10} M$_\odot$ from Licquia & Newman (2015). For the latter, we adopt a double exponential form describing the separate thin- and thick-disc components. We take the scale radii of the thin- and thick-discs to be $R_t = 2.5$ kpc and $R_T = 2.0$ kpc with a surface density ratio at $R_{gal} = 0$ of $\Sigma_T/\Sigma_t = 0.27$ based on the findings of Bland-Hawthorn & Gerhard (2016).

• The Johnson et al. (2021) models run VICE in star formation mode, meaning that the user specifies the SFH and the amount of gas and infall at each timestep are calculated automatically by the code. Determining the gas supply requires an assumption about the star formation law (often referred to as "star formation efficiency" in the chemical evolution literature, though this term has other meanings in, e.g., the star formation and feedback community). Previously, GCE models have adopted a single power-law relating Σ_{gas} and $\dot{\Sigma}_\star$ based on the findings of Kennicutt (1998), but recent studies have revealed that the star formation law on a galaxy-by-galaxy basis is much more nuanced (de los Reyes & Kennicutt 2019; Ellison et al. 2021; Kennicutt & de los Reyes 2021), and some of the uncertainty regarding its details can be traced back to the ongoing debate about the CO-to-H$_2$ conversion factor (Kennicutt & Evans 2012; Liu, Gao & Greve 2015). Based on a compilation of the Bigiel et al. (2010) and Leroy et al. (2013) data shown in comparison to the theoretically motivated star formation laws of Krumholz et al. (2018, see their Fig.

2), Johnson et al. (2021) take a three-component power-law as their star formation law with the index given by:

$$N = \begin{cases} 1.0 & (\Sigma_{gas} \geq 2 \times 10^7 \text{ M}_\odot \text{ kpc}^{-2}) \\ 3.6 & (5 \times 10^6 \text{ M}_\odot \text{ kpc}^{-2} \leq \Sigma_{gas} \leq 2 \times 10^7 \text{ M}_\odot \text{ kpc}^{-2}) \\ 1.7 & (\Sigma_{gas} \leq 5 \times 10^6 \text{ M}_\odot \text{ kpc}^{-2}). \end{cases} \quad (5)$$

The normalization of the star formation law is then set by letting the SFE timescale $\tau_\star \equiv \Sigma_{gas}/\dot{\Sigma}_\star$ be given by the value derived observationally for molecular gas at surface densities where $N = 1$. The value of $\tau_\star$ for molecular gas at the present day is taken to be $\tau_{mol,0} = 2$ Gyr (Leroy et al. 2008, 2013) with a $t^{1/2}$ time-dependence based on the findings of Tacconi et al. (2018) studying the $\Sigma_{gas} - \dot{\Sigma}_\star$ relation as a function of redshift.

• Because of the yields adopted in the Johnson et al. (2021) models, considerable outflows are required in order to predict plausible abundances. Weinberg et al. (2017) demonstrate analytically that to first order the equilibrium abundance of some element in the ISM is determined by its yield and the mass-loading factor $\eta = \dot{\Sigma}_{out}/\dot{\Sigma}_\star$ with a small correction for the SFH. Johnson et al. (2021) make use of this to select a scaling of η with R_{gal} such that the equilibrium abundance as a function of radius corresponds to a reasonable metallicity gradient within the Galaxy (see their Fig. 3 and discussion in § 3.1).

4 RESULTS

4.1 Evolution of a Fiducial Model

• Our fiducial model adopts, together with the supernova yields of Johnson et al. (2021, see discussion in § 3), $y_N^{CC} = 3.6 \times 10^{-4}$ and the C11+C15 AGB star yield tables.

• In the left panel of Fig. 5, we plot the evolution of the N and O abundances in the gas phase in five rings at a range of Galactocentric radii. At early times, [O/H] is low and [N/O] reflects the ratio of the CCSN yields ([N/O] ≈ −0.7). As the Galaxy evolves, AGB stars begin enriching the ISM with their N yields, and [N/O] increases. Being an element produced primarily by CCSNe on short delay times, O reaches an equilibrium abundance on timescales of a ∼few Gyr (Weinberg et al. 2017), and consequently the metallicity gradient in [O/H] is established soon after AGB stars begin producing N. [N/O] then continues to increase at an approximately fixed [O/H] due to the ongoing N production in AGB stars. As a consequence, the gas phase tracks in the [N/O]-[O/H] plane are unique from one another at different radii.

• Because there is a delay between a stellar population's formation and N production from its AGB stars (∼250 Myr in this model; see Fig. 4), stellar migration can occur in this time interval. Although the bulk of migration occurs on longer timescales, this characteristic delay time is comparable to the dynamical time of the Milky Way and is thus an adequate amount of time for kinematic heating to at least begin. As a consequence, there may be a slight deficit or surplus of N-producing AGB stars in a given ring at some time induced by stellar migration. These tracks can thus move vertically in this plane in response to stars moving between rings as the Galaxy evolves, entirely independent of the SFH and the nucleosynthetic yields of stars that formed in any given ring. We demonstrate this effect by comparing the solid blue and purple lines to their dotted counterparts, which denote the tracks when we neglect stellar migration entirely (i.e. the "post-processing" model from Johnson et al. 2021). This is similar to what Johnson et al. (2021) found for SN Ia enrichment of Fe (see discussion in their §§ 3.2 and 3.4).

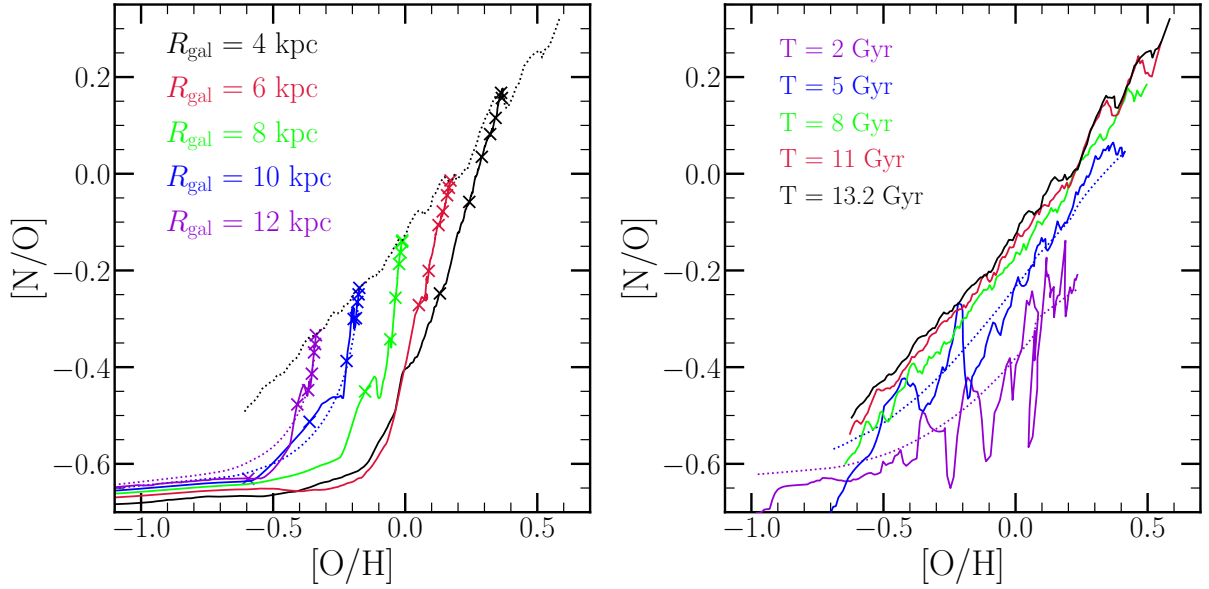• This panel also suggests that the [N/O]-[O/H] relation arises as

Figure 5. *Left*: The gas-phase [N/O]-[O/H] relation parameterized by time at fixed radius (solid coloured lines) in the fiducial model. X's denote the abundances at T = 2, 4, 6, 8, 10, 12, and 13.2 Gyr (the present day) at these radii. The dotted blackcline is the same as the solid black line in the right panel. Coloured dotted lines mark the evolution of our model at R_{gal} = 10 and 12 kpc when stellar migration is neglected. *Right*: The gas-phase [N/O]-[O/H] relation parameterized by radius at various snapshots (solid coloured lines) in our fiducial model with the C11+C15 yields. Similar to the left hand panel, coloured dotted lines denote the resulting relation at T = 2 and 5 Gyr when we neglect stellar migration.

a superposition of endpoints rather than an evolutionary sequence. Rather than each ring's track passing through a well-defined region of abundance space, they instead evolve upward more or less parallel to one another (modulo the effect of stellar migration). This is a direct consequence of the fact that the [O/H] abundances approach equilibrium quickly, and changes in the [N/O] ratio thereafter almost entirely reflect changes in the N abundances; the result is an [N/O]-[O/H] relation that reflects the Galaxy's metallicity gradient more so than different evolutionary states. Similar arguments have been made regarding the low [α/Fe] stars in the Galaxy (e.g. Schönrich & Binney 2009; Sharma et al. 2020).

• In the right panel of Fig. 5, we plot the gas-phase [N/O]-[O/H] relation predicted by the model at various snapshots. To obtain this, we simply take the N and O abundances in the ISM at a given snapshot for each δR_{gal} = 100 pc ring at R_{gal} > 2 kpc and plot them as a line. The relation is generally time-independent after $T \gtrsim 5$ Gyr, though there is some evolution toward higher [N/O]. We again demonstrate the impact of stellar migration by comparing the solid blue and purple lines to their dotted counterparts, which quantify the relation when we neglect migration. This indicates that the complex features seen in the relation at all times is an effect of stellar migration as discussed above.

• Johnson et al. (2021) found that the SN Ia rate in this model can vary by as much as a factor of ~3 at large radii ($R_{gal} \gtrsim 9$ kpc), also as a consequence of stellar migration (see their Fig. 8 and discussion in their § 3.4). They demonstrate that this is a sufficiently large effect such that the resultant stellar populations are Fe-poor enough to explain the intrinsically young sub-component of the young α-rich stars observed in the solar neighbourhood with APOGEE[1] (see discussion in their §§ 3.2 and 3.4; Chiappini et al. 2015; Martig et al. 2015, 2016;

Jofré et al. 2016; Yong et al. 2016; Izzard et al. 2018; Silva Aguirre et al. 2018; Warfield et al. 2021). For N, the effect is much smaller ($\lesssim 0.1$ dex), but there are some instances at early times where the impact of stellar migration is more substantial. The smaller effect on N enrichment rates can be understood from the relative timescales of their production (see Fig. 4 and discussion in § 2.3). Produced on timescales of a ~couple hundred Myr, N yields are ejected from stellar populations ~5 times faster than Fe (even faster in our alternate AGB star yield models). Consequently, there is much less time for stellar migration to occur within the timescale of N production than there is within the timescale of Fe production, and as a result, migration has only a small impact on the gas phase N abundances. This underscores the argument from Johnson et al. (2021) that in order for nucleosynthetic yields to migrate significant distances along with their progenitor stellar populations, the timescale for production needs to be at least comparable to the migration timescale.

4.2 Comparison to Observed Gas Phase Trends

• We use the Dopita et al. (2016) measurements as our observational baseline. They are a good representation of many results for gas phase N and O abundances, and they agree well with APOGEE stellar trends (Vincenzo et al. 2021).

• The left hand panel of Fig. 6 compares the predictions of our model made with each of the AGB star yield models discussed in § 2.2 and visualized in Fig. 3.

• The model fails to reproduce the gas phase [N/O]-[O/H] relation as observed with all published yield tables. The C11+C15 and V13 yields are able to reproduce the qualitative trend, but with an incorrect normalization. The K10 and KL16+K18 yields, on the other hand, fail to reproduce the steadily sloped increase of [N/O] with [O/H].

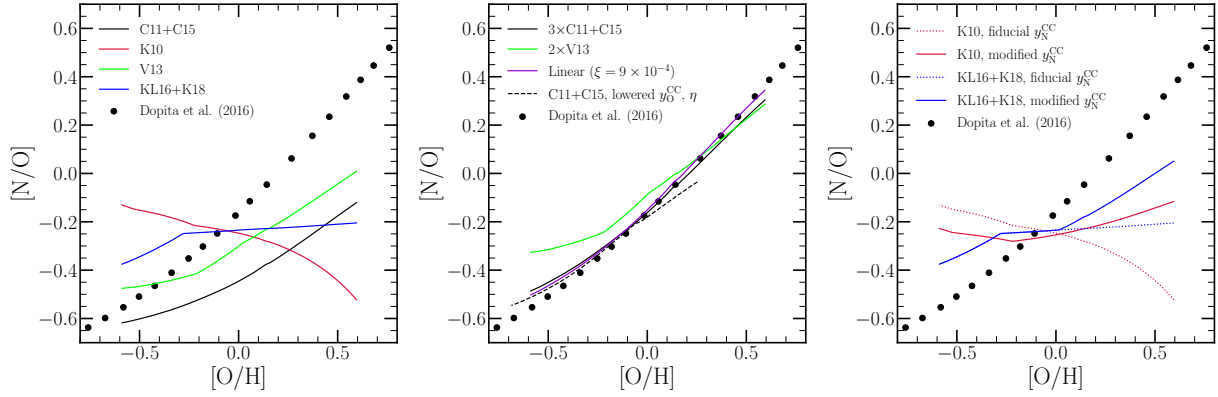– In the case of K10, the model overpredicts [N/O] at low [O/H]

Figure 6. Left: The present day gas-phase [N/O]-[O/H] relation predicted by our model with each of the four yield models based on stellar evolution models discussed in § 2.2, colour-coded according to the legend. We include the Dopita et al. (2016) measurements of this relation for local stars and HII regions (duplicated from Fig. 1) as the observational benchmark. **Middle**: The same as the left panel, but for a case where we artificially amplify the C11+C15 yields by a factor of 3 and the V13 yields by a factor of 2. Since our linear model is also based on the C11+C15 yields, we in turn amplify the slope from $\xi = 3\times10^{-4}$ as shown in Fig. 3 to $\xi = 9 \times 10^{-4}$ and include it here as well. **Right**: The same as the left panel, but comparing the predictions made by the K10 and KL16+K18 yields with our fiducial value of y_N^{CC} (dotted lines, same as left-hand panel) to those with the alternate forms of y_N^{CC} (solid lines) given by equation (6) for the K10 yields and equation (7) for the KL16+K18 yields.

and predicts [N/O] to *decrease* monotonically with increasing [O/H]. With a slope of the wrong sign, there is no multiplicative factor by which we can amplify or suppress these yields in order to reproduce the observations.

– The KL16+K18 yields improve upon the K10 predictions to some extent. The overprediction of [N/O] at low [O/H] is largely corrected, but it predicts a relatively flat trend of [N/O] above [O/H] $\gtrsim -0.2$, leading still to an underprediction of [N/O] at high [O/H].

• In order to successfully reproduce the observations, we find that we need to artificially amplify the C11+C15 and V13 yields by factors of ~3 and ~2, respectively. Having originally comparing our linear model to the C11+C15 yields in Fig. 3 with $\xi = 3 \times 10^{-4}$, we amplify the value of ξ by a factor of 3 here as well. We show the results of these modified yield models in the middle panel of Fig. 6. Although the V13 model predict an [N/O]-[O/H] relation that is slightly shallower than the Dopita et al. (2016) measurements, the predictions are reasonably within the scatter seen in Fig. 1.

– Although the C11+C15 and V13 yield models fail under our fiducial model, they're successful if we lower both y_O^{CC} and our outflow mass loading factor η as a function of R_{gal} by factors of 3 and 2, respectively. These parameters, which approximately determine the equilibrium abundance in a one-zone model (Weinberg et al. 2017), are tuned to reproduce a metallicity gradient in the disc which resembles that observed for the Milky Way (see discussion in § 2.4 of Johnson et al. 2021). However, since the yield and the outflow are simply source and sink terms, the model makes similar predictions when both are lowered by the same factor. We demonstrate this in the middle panel with the black dashed line for the C11+C15 yield model with both y_O^{CC} and η lowered by a factor of 3. This model spans a different range in [O/H] because the relation between y_O^{CC} and η isn't exactly one-to-one, but the predictions still lie in the same region of the [N/O]-[O/H] plane.

– Because the enrichment rates are the same, we find similar results if we simply add a portion of the SN yields (both CCSN and SN Ia) to the outflow while also lowering η at all radii. Vincenzo et al. (2016a) are also able to reproduce the [N/O]-[O/H] relation in chemical evolution models by implementing a differential wind

in which outflows remove O but not N from the star forming reservoir. Because of the close relation between the yields and the outflows in establishing the present day abundances, this is also similar to simply lowering the adopted O yields from CCSNe.

– Lowering our SN yields by a factor of $2 - 3$ is plausible if a substantial fraction of massive stars collapse directly to black holes as opposed to exploding as SNe. Our IMF-averaged massive star yields are based on a Kroupa (2001) IMF combined with SN nucleosynthesis models in which most $M > 8M_\odot$ stars explode as a CCSN (e.g. Woosley & Weaver 1995; Chieffi & Limongi 2004, 2013; Limongi & Chieffi 2006; Nomoto et al. 2013). The criteria for massive star explosions and whether or not these "failed supernovae" indeed occur in nature has been a recent topic of interest from both theoretical (e.g. Pejcha & Thompson 2015; Sukhbold et al. 2016; Ertl et al. 2016) and observational perspectives (e.g. Gerke, Kochanek & Stanek 2015; Adams et al. 2017; Basinger et al. 2021). At present, no combination of a SN nucleosynthesis model with a physically motivated black hole landscape is able to reproduce the observed abundance patterns (Griffith et al. 2021). Despite this, black hole formation still lowers SN yields by simply not ejecting the nucleosynthetic products to the ISM and is thus an alternate explanation for the failure of our fiducial model to reproduce the observed [N/O]-[O/H] relation with the C11+C15 and V13 yield models.

• Can an alternate parameterization of y_N^{CC} reproduce the observations with the K10 and KL16+K18 AGB star yield models?

– If the K10 yields are to reproduce the observations, the overall N abundance must decrease at low [O/H] and increase at high [O/H]; one way to do this is with a metallicity-dependent CCSN yield. We therefore construct the following parameterization of y_N^{CC}:

$$y_N^{CC} = (3.6 \times 10^{-4}) \left(\frac{Z}{Z_\odot} \right). \tag{6}$$

We illustrate this model with the slanted black dotted in Fig. 2. While our fiducial model best describes the rotating CCSN models of Limongi & Chieffi (2018), this alternate parameterization follows the non-rotating models published in Limongi & Chieffi

(2018), Sukhbold et al. (2016), Nomoto et al. (2013), and Woosley & Weaver (1995) while maintaining the same base-line value of 3.6×10^{-4} at solar metallicity.

– If the KL16+K18 yields are to reproduce the observed results, then contrary to the predictions made with the K10 yields, the overall N abundance at low [O/H] is fine. Instead, it's only the N abundance at high [O/H] that needs correcting. We therefore construct a second alternate form of y_N^{CC} by retaining the value of the fiducial yield at sub-solar metallicity but assuming the value of equation (6) above solar metallicity:

$$y_N^{CC} = \begin{cases} 3.6 \times 10^{-4} & (Z \leq Z_\odot) \\ (3.6 \times 10^{-4})\left(\frac{Z}{Z_\odot}\right) & (Z \geq Z_\odot). \end{cases} \tag{7}$$

– We compare our model predictions with these alternate CCSN yields for the K10 and KL16+K18 AGB star yields in the right hand panel of Fig. 6. These modifications are able to make up some of the difference, but both models still predict an [N/O]-[O/H] relation that is simply too shallow to explain the observations.

· The inverse dependence of [N/O] with [O/H] when taking the K10 yields can be understood by the interaction between TDU and HBB (see discussion in § 2.2). Both effects are stronger at low metallicity, and since all of the K10 models experiencing HBB also experience TDU (see their Table 1), such a result is not surprising. This is also true for the KL16+K18 yields, but that model predicts a relatively flat [N/O]-[O/H] relation owing to differences in the ^{14}N yields as a consequence of updated model inputs (see discussion in § 2.2).

· Despite these results, we cannot say with any confidence whether or not such a wide mass range of stars should experience both TDU and HBB. Although this makes it difficult for the model to predict a monotonic increase in [N/O] with [O/H], there are many uncertain parameters required to predict yields with stellar evolution models, and we have only investigated a few of them here.

• In short, in order to reproduce the gas-phase [N/O]-[O/H] relation as observed, our model requires N yields which increase monotonically with metallicity in a manner similar to what we illustrate in the right panel of Fig. 4 for the C11+C15, V13, and linear models. With the C11+C15 and V13 models specifically, our results suggest that these yields must increase by factors of $2 - 3$ or that many massive stars must collapse directly to black holes; it may also be a mix of the two. With our models, the only other way to achieve good agreement would be to adopt a metallicity-dependent CCSN yield of O. Supernova nucleosynthesis models, however, would dispute such an assumption (e.g. Woosley & Weaver 1995; Nomoto et al. 2013; Limongi & Chieffi 2018), and there is some empirical evidence that the metallicity dependence of the O yield is minimal at most (Weinberg et al. 2019, 2021).

• Despite predicting a different mass dependence for y_N^{AGB} (see Fig. 3), the C11+C15 and V13 yield models both reproduce the slope of the [N/O]-[O/H] relation reasonably well. This is an indication that perhaps the metallicity dependence plays a much more important role then the time dependence in establishing this correlation. To investigate this further, we consider two variations of our fiducial model: one with the time dependence removed from the enrichment rate calculations, and the other with the metallicity dependence removed.

• To remove the time dependence, we make use of VICE's capability to let the user specify functional forms for nucleosynthetic yields.
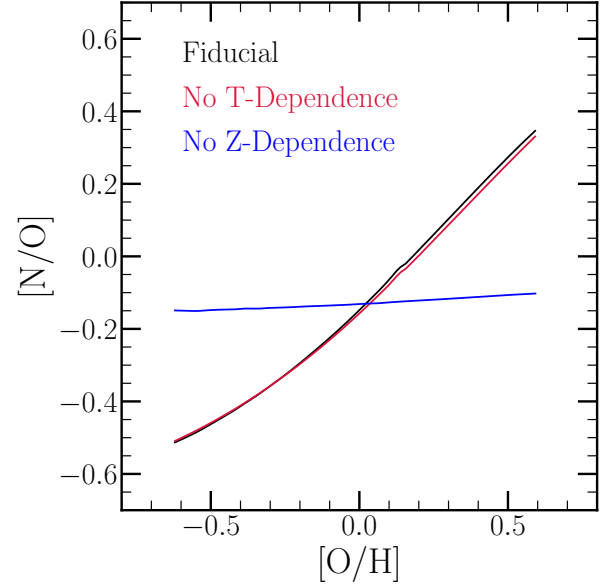

Figure 7. A comparison between our fiducial model with post-processing migration (black) and variations with the time dependence (red) and metallicity dependence (blue) removed. To remove the time dependence, we pre-compute the yields of N from 13.2 Gyr old single stellar populations as a function of metallicity as in the right panel of Fig. 4, then incorporate this into the prompt CCSN yields and set the delayed AGB star contribution to zero. To remove the metallicity dependence, we evaluate the yields at our assumed solar metallicity of $Z = 0.014$ at all timesteps.

We pre-compute the N yield from all AGB stars associated with a 13.2 Gyr old stellar population as a function of progenitor metallicity in the same fashion as in the right panel of Fig. 4. Since VICE works from IMF-averaged CCSN yields assumed to be injected instantaneously following a single stellar population's formation, we simply add this N yield to y_N^{CC} and set y_N^{AGB} equal to zero. In this model, y_N^{CC} inherits a metallicity-dependence from the AGB star yields and has the exact shape as the curves in the right hand panel of Fig. 4.

• To remove the metallicity dependence, the procedure is much simpler: we simply evaluate y_N^{AGB} at our assumed solar metallicity of $Z = 0.014$ at all timesteps. In this model, there is still a delay-time distribution to AGB star N production inherited from the stellar mass-lifetime relation.

• We illustrate the results of this process in Fig. 7. The model with no time-dependence is nearly identical to the [N/O]-[O/H] relation found in our fiducial model, while the model with no metallicity-dependence is considerably different. This suggests that the metallicity dependence indeed plays a much larger role than the DTD in establishing the overall shape of the [N/O]-[O/H] relation. This is rather unsurprising given the short characteristic timescales of N production by AGB stars ($\lesssim 200$ Myr, see the middle panel of Fig. 4). Mathematically, there is little difference in the enrichment rates if all of a stellar population's N is produced immediately as opposed to with a sharply declining DTD. The metallicity dependence, however, is paramount to the [N/O]-[O/H] relation, which is expected given the results in Fig. 3.

• We clarify that we are making this claim *only* for N and not for any other elements produced in AGB stars. The time-dependence of AGB star enrichment is dictated by both the stellar mass-lifetime relation and the mass-dependence of the yields from AGB stars. Because different elements are produced in different amounts by AGB
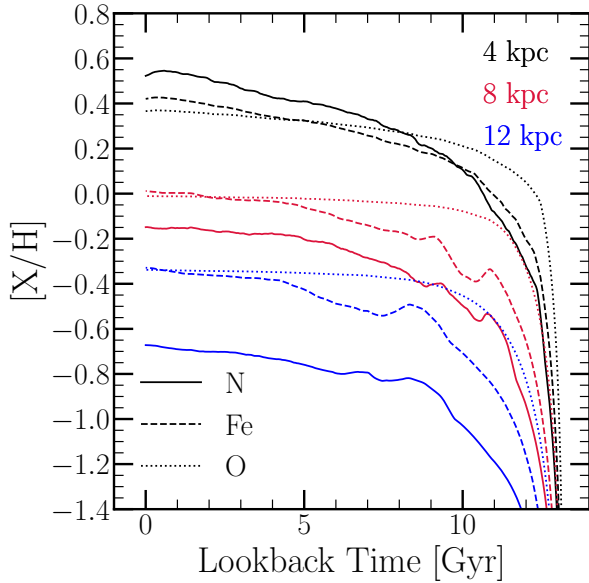
Figure 8. [N/H] (solid), [Fe/H] (dashed), and [O/H] (dotted) in the gas phase as a function of lookback time in the fiducial model at R_{gal} = 4 (black), 8 (red), and 12 kpc (blue).

stars of different masses, the AGB star DTD is generally different from element to element. N is somewhat unique in that its yields are dominated by high mass AGB stars (see, e.g., Fig 4 here for N in comparison to Fig. 5 of Johnson & Weinberg 2020 for strontium). We caution against interpretations of AGB star nucleosynthesis which attribute a single characteristic delay-time to this enrichment channel as it may lead to spurious conclusions.

4.3 Comparison to Stellar Abundances in the Milky Way Disc

• Before comparing the predictions of GCE models to observational data, it is essential that the N abundances be adjusted to account for internal processes that alter the surface compositions of stars. This is an important step to take before comparing GCE models to observational data, because GCE models predict the birth abundances of stars, and N abundances in evolved stars do not reflect their birth abundance. After the CNO cycle has processed much of the C and O nuclei into ^{14}N during a star's main sequence lifetime, this N-rich material from the core is mixed with the outer convective layers, increasing the N abundance in the photosphere. Using MESA stellar evolution models (Paxton et al. 2011, 2013, 2015, 2018) with standard mixing prescriptions, Vincenzo et al. (2021) developed a prescription to approximate the birth abundances of C, N, and O and apply it to a sample of APOGEE/Kepler red giants. They find good agreement between the APOGEE abundances and the Dopita et al. (2016) measurements, so the fiducial model's successful reproduction of the Dopita et al. (2016) trend is an indication that it also successfully reproduces the overall trend of [N/O] vs. [O/H] found for APOGEE disc stars. In this section we focus on the stellar abundances, with which we can investigate trends with age and [O/Fe].

• In Fig. 8, we plot the evolution of the N, O, and Fe abundances in the gas phase at the R_{gal} = 4, 8, and 12 kpc rings in our fiducial model. [N/H] is more correlated with [Fe/H] than [O/H] at all radii, and the relation persists up to lookback times of ~10 Gyr. This arises in part because N and Fe are both produced in significant quantities

by delayed enrichment sources while O is produced almost entirely on short timescales by CCSNe (see discussion in § 2). Although the production timescale of N from single stellar populations is short compared to Fe (see discussion in § 2.3), metallicity dependent yields require more abundant species such as O and Fe to be produced and reach an equilibrium before N yields stabilize. When many stellar populations are present, N abundances are thus somewhat limited in how fast they can increase due to the metallicity dependent nature of AGB star yields; Johnson & Weinberg (2020) found similar results regarding Fe and strontium (Sr). As a consequence of its single dominant nucleosynthetic source with a metallicity-independent yield, O reaches an equilibrium abundance on much shorter timescales than elements like N and Fe which have significant contributions from delayed sources (Weinberg et al. 2017); because of this, [O/H] is nearly independent of lookback time as far back as ~10 Gyr ago while [N/H] and [Fe/H] are not.

• In the left hand panel of Fig. 9, we compare our model predictions to their [N/O] abundances with the ages taken from Miglio et al. (2021). The model correctly predicts that the [N/O]-age relation is relatively flat in bins of [Fe/H]. This arises as a consequence of the N-Fe correlation described in Fig. 8: a bin in [Fe/H] is also approximately a bin in [N/H], and with [O/H] more or less constant, the [N/O]-age relation at fixed [Fe/H] is relatively flat up to ages of ~10 Gyr. This is an important success of the model, because with uncorrected N abundances, [N/O] vs. age exhibits a significant negative slope at fixed [Fe/H] (see Fig. 7 of Vincenzo et al. 2021). Our model does, however, slightly underpredict [N/O] in the [Fe/H] = −0.2 − 0 bin. In general, our model occupies a wider range in [N/O] at all ages than does the Vincenzo et al. (2021) measurements, suggesting that our yields scale with metallicity slightly too strongly.

• In the right panel of Fig. 9, we compare our model predicted [N/O]-[O/Fe] relation to their calculations. As in the left hand panel, our model predicted stellar populations occupy a wider range of [N/O] than the data, but the agreement is otherwise good. The model correctly predicts that [N/O] should increase with decreasing [O/Fe] at all metallicities. This anti-correlation is also a direct consequence of the N-Fe correlation: as the two abundances increase together in the ISM, [N/O] increases and [O/Fe] decreases. This is also an important success of the model; Vincenzo et al. (2021) demonstrate that when stellar N abundances are corrected for internal mixing process, the dichotomy between the chemical thin and thick discs persists for this element.

4.4 The Sources of Scatter in the [N/O]-[O/H] Relation

• Schaefer et al. (2020) demonstrate that intrinsic scatter in the gas phase [N/O]-[O/H] relation in MaNGA galaxies is correlated with variations in the local SFE. This is expected from simple GCE models: with slower star formation, more AGB stars enrich the ISM by the time it reaches a given abundance, causing a higher [N/O] at fixed [O/H]. However, they do not rule out radial migration as another potential source of scatter in this relation. Our models, taking into account the effects of radial migration on the enrichment rates and thus the gas phase abundances, are the ideal tool with which to address this question.

• We construct two additional extensions of our fiducial model, one in which the SFE exhibits 25% sinusoidal variations in time, and the other with the same 25% variations in the SFR. We modify the SFE timescale $\tau_\star$ and SFH $\dot{\Sigma}_\star$ from the fiducial case in the following manner:

$$\tau_\star(R_{gal}, t) = \tau_{\star,J21}(R_{gal}, t)\left(1 + 0.25\sin\left(\frac{2\pi t}{2\text{ Gyr}}\right)\right) \quad (8)$$

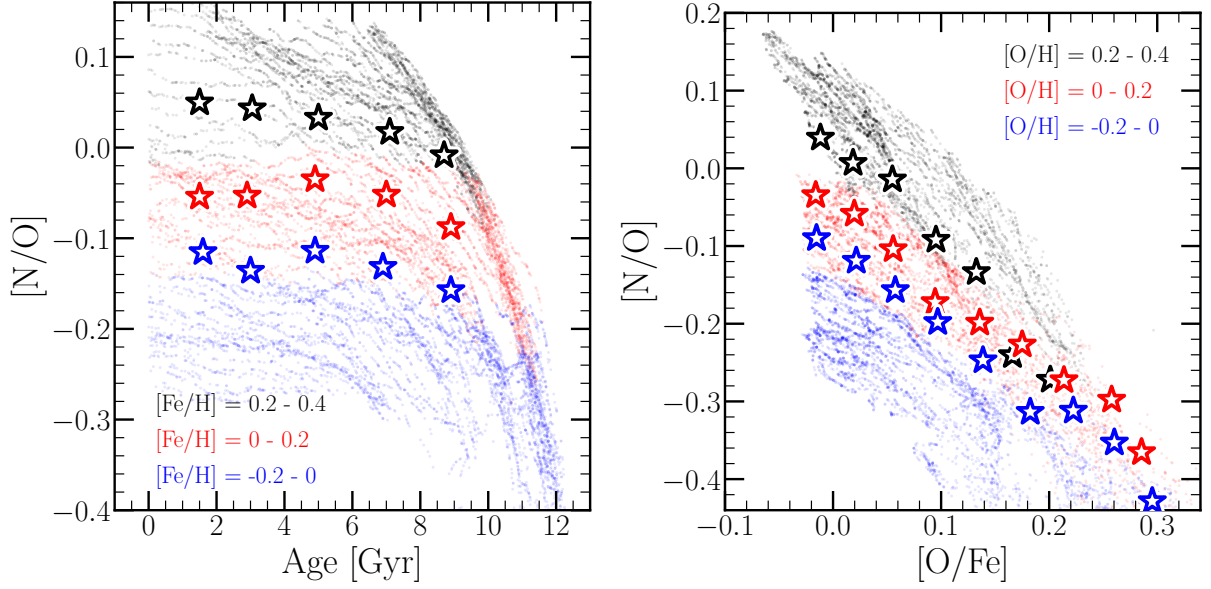**Figure 9. Left**: [N/O] as a function of stellar age for 5000 stars randomly sampled from our model stellar populations in three bins of [Fe/H] (colored points). Stars quantify the median trend of [N/O] with age corrected for internal mixing in the same bins of [Fe/H] from the Vincenzo et al. (2021) sample. **Right**: The same as the left hand panel, instead showing [N/O] as a function of [O/Fe] in bins of [O/H].
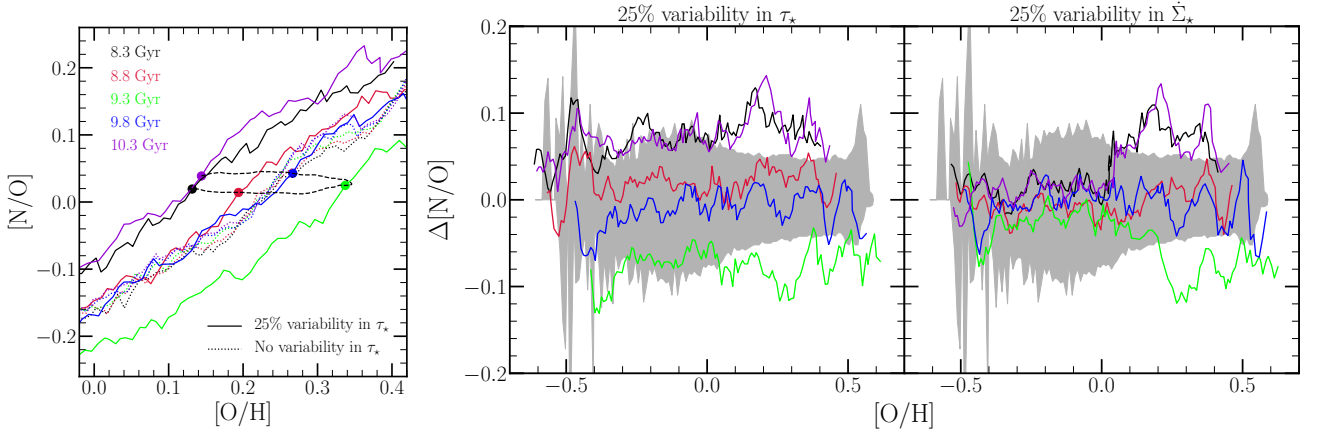

Figure 10. Left: One cycle of oscillations in the [N/O]-[O/H] relation at high [O/H] induced by 25% sinusoidal variability in $\tau_\star$ (solid coloured lines). Dotted lines show the [N/O]-[O/H] relation at the same five snapshots in the fiducial model with no variability in $\tau_\star$. The black dashed line shows the time evolution of the abundances in the R_{gal} = 5 kpc ring, with the times of each of the five snapshots marked by a coloured point. **Middle and Right**: For the same five snapshots in the left hand panel, the deviation in [N/O] at fixed [O/H] relative to the fiducial model for the case with 25% variability in $\tau_\star$ (middle) and in $\dot{\Sigma}_\star$ (right). The shaded regions in both panels quantify the width of the [N/O] distribution in $10^{10.5} - 10^{11}$ M$_\odot$ galaxies in MaNGA taken from Schaefer et al. (2020). The median [N/O] is placed at Δ[N/O] = 0, and the lower (upper) envelope denotes the 16th (84th) percentile of the [N/O] distribution at a given [O/H].

$$\dot{\Sigma}_\star(R_{gal}, t) = \dot{\Sigma}_{\star, J21}(R_{gal}, t) \left(1 + 0.25 \sin\left(\frac{2\pi t}{2 \text{ Gyr}}\right)\right), \quad (9)$$

where $\tau_{\star, J21}$ and $\dot{\Sigma}_{\star, J21}$ refer to the SFE timescale and SFH in the fiducial model taken from Johnson et al. (2021). In h277, the simulation from which the migration history for our model is drawn, we find that the overall SFE declines by a factor of ~2 over the past ~9 Gyr, an effect which is already built into $\tau_{\star, J21}$. Additionally, there are variations in the SFE at the ~25% level between similar radii in the same snapshot as well as at fixed radii between successive snapshots. Based on this, an amplitude of 25% should capture typical variations seen in these quantities in hydrodynamical simulations. However,

since h277 has a remarkably quiescent merger history (Zolotov et al. 2012), this may change in reponse to a major accretion event. (If it's worth it, we could add a sentence here with a couple of observational references.)

• In a real galaxy, variability in the SFE and the SFR is likely non-sinusoidal and not with constant amplitude. When observing a sample of galaxies, they will have different amplitudes and be seen at different phases in their variability, and the impact of this on their N and O abundances will present as intrinsic scatter in the inferred trend. By comparing models with and without reasonable amounts of variability while taking into account stellar migration, we can assess which quantities impact abundances more strongly and are thus the

more likely causes of intrinsic scatter in the observed [N/O]-[O/H] relation.

• In the left panel of Fig. 10, we plot the predicted gas-phase [N/O]-[O/H] relation at high [O/H] for five snapshots covering one cycle of the fluctuations induced by variability in $\tau_\star$. This model predicts a ~0.15-dex dynamic range in [N/O] at fixed [O/H], whereas the model with no variability in $\tau_\star$, denoted by the dotted lines, predicts the relation to be nearly constant in comparison over this time interval. Because both models include the effects of stellar migration, we therefore argue that reasonable variability in the local SFE is a more likely source of intrinsic scatter in the gas phase [N/O]-[O/H] relation; we find similar results for varability in the SFR.

• Such behavior is driven by the constant tug-of-war between dilution and re-enrichment associated with oscillations in $\tau_\star$. In this model, $\dot{\Sigma}_\star$ is the same as it was in Johnson et al. (2021), so it is not the SFR which varies but rather the gas supply. When the gas supply increases, the ISM becomes diluted, decreasing [O/H]. Because the AGB star yields of N with our fiducial C11+C15 model are roughly linear with metallicity, the decrease in the N abundance due to the now lowered yields are in direct proportion to the amount of dilution but with a slight delay. As a result, [N/O] is only marginally affected by the fluctuations in the overall abundance. The variations in the [N/O]-[O/H] relation that the model predicts are therefore more of a consequence of variability in [O/H] than in [N/O]. We demonstrate this with the black dashed line in the left hand panel of Fig. 10, which traces out the evolution of the abundances at $R_{\rm gal}$ = 5 kpc over the same time interval. In general, [N/O] is affected only at the ~0.05-dex level while [O/H] varies with an amplitude of ~0.25-dex. As the gas supply falls off, enrichment proceeds in a gas-starved ISM, which increases [O/H] once more, but [N/O] to a lesser extent for similar reasons, and the cycle repeats itself.

• When $\dot{\Sigma}_\star$ varies, $\Sigma_{\rm gas}$ and consequently the abundances vary instead at a value of $\tau_\star$ that varies only as much as the adopted $\dot{\Sigma}_\star - \Sigma_{\rm gas}$ relation from Johnson et al. (2021) dictates it should (see discussion in § 3), with no additional variations in time.

• In the middle and right hand panels of Fig. 10, we plot the difference in [N/O] at fixed [O/H] between the fiducial model and those with variability (i.e. the vertical offset between the solid and dotted curves in the left hand panel). Both scenarios produce offsets in [N/O] at high [O/H] (which as discussed above are more offsets in [O/H] at fixed [N/O]), but the model with variations in $\dot{\Sigma}_\star$ does not predict any significant fluctuations in the abundances at [O/H] $\lesssim -0.2$. This difference is a consequence of the mathematical form of $\tau_{\star,\rm J21}$ (see discussion in § 3) and the fact that these models run VICE in star formation mode. The low [O/H] end of this relation arises from large $R_{\rm gal}$ due to the metallicity gradient, and the surface densities of gas our model predicts at these radii are in the $\dot{\Sigma}_\star \propto \Sigma_{\rm gas}^{3.6}$ portion of the adopted $\dot{\Sigma}_\star - \Sigma_{\rm gas}$ relation. However, since these models run from a specified SFH, it's not that the SFH is a strong function of the gas supply but rather that the gas supply is a weak function of the SFH. As a consequence, 25% oscillation in $\dot{\Sigma}_\star$ therefore have little impact on the ISM gas supply; there is then a minimal impact on abundances since the effect of dilution is greatly minimized. At smaller $R_{\rm gal}$ (i.e. higher [O/H]), $\Sigma_{\rm gas}$ varies more strongly with $\dot{\Sigma}_\star$, and as expected the impact on abundances is more significant. If we were to adopt an alternate form of the $\dot{\Sigma}_\star - \Sigma_{\rm gas}$ relation, such as a purely linear or single power-law formalism as in many GCE studies, then this effect would be seen at all [O/H] when $\dot{\Sigma}_\star$ oscillates. Alternatively, we expect similar results if we were to run an equivalent model with VICE in infall mode (i.e. specifying the infall history and initial gas supply rather than the SFH).

• The shaded regions in the left and middle panels of Fig. 10 quantify the scatter in the gas-phase [N/O]-[O/H] relation inferred observationally by Schaefer et al. (2020). Using data from Mapping nearby Galaxies at Apache Point Observatory (MaNGA; Bundy et al. 2015), an integral field unit survey, they measure N and O abundances in 709,541 spaxels across 6,507 unique galaxies spanning a stellar mass range from $10^9 - 10^{11}$ M$_\odot$. Since our model is appropriate for Milky Way mass galaxies, we focus our comparison on the $M_\star = 10^{10.5} - 10^{11}$ M$_\odot$ range, which cuts our sample to 197,787 individual N and O measurements from the MaNGA IFU spaxels. In narrow bins of [O/H], we then compute the median [N/O] as well as the 16th and 84th percentiles of the [N/O] distribution. Placing the median [N/O] at Δ[N/O] = 0, the shaded regions above and below 0 in Fig. 10 denote the difference between the 16th and 84th percentile of the distribution in each bin.

• Our models with 25% sinusoidal oscillations in $\dot{\Sigma}_\star$ and $\tau_\star$ produce deviations in [N/O] at fixed [O/H] that are comparable to the width of the distribution measured observationally. Stellar migration, on the other hand, induces only small variations, as can be seen in the left-hand panel of Fig. 10. This traces back to the timescales of N production from single stellar populations (see Fig. 4 and discussion in § 2.3): most N production occurs quickly following a stellar population's formation (~few hundred Myr), meaning that most stars will not migrate far from their birth radius by the time they produce their N, and the resulting impact on the gas phase abundances is minimal.

• These results support the conjecture from Schaefer et al. (2020) that the correlation between the local SFE and scatter in the [N/O]-[O/H] relation is indicative of a causal relationship. However, our models suggest that variations in the SFR can also produce similar scatter in the relation. Although it is difficult to disentangle the two because the SFR and the SFE are also correlated (i.e. the $\dot{\Sigma}_\star - \Sigma_{\rm gas}$ relation; e.g. Kennicutt 1998; de los Reyes & Kennicutt 2019; Kennicutt & de los Reyes 2021), the SFR can also vary as a consequence of, e.g., variations in the accretion rate from the intergalactic medium. Such a phenomenon induces the effects of dilution which we demonstrate here to be the primary source of variability and thus scatter in the [N/O]-[O/H] plane.

5 CONCLUSIONS

• We have made use of the GCE models from Johnson et al. (2021) which characterize the Milky Way disc as a series of concentric rings with a uniform $\delta R_{\rm gal}$ = 100 pc width. These models treat each individual ring as a conventional one-zone model of chemical evolution while allowing individual stellar populations to move between rings to include the effects of stellar migration.

• We retain the IMF-averaged CCSN and SN Ia yields of O and Fe from Johnson et al. (2021), adopt a zero yield of N from SN Ia, and investigate theoretical and empirical CCSN N yields. If our CCSN yield of O is accurate ($y_{\rm O}^{\rm CC} = 0.015$), then the CCSN yield of N required to produce the "plateau" of [N/O] = -0.7 at low [O/H] is $y_{\rm N}^{\rm CC} = 3.6 \times 10^{-4}$. Of the recent CCSN nucleosynthesis investigations, only Limongi & Chieffi (2018) present yields for rotating progenitors. With the non-rotating models falling short of this value, we find that the effects of rotation are necessary to explain the N abundances seen at low [O/H], consistent with recent results from Grisoni et al. (2021).

• There are substantial differences between the mass- and metallicity-dependencies of the AGB star yields of N predicted from theoretical models (see Fig. 3). Although ascertaining the origins of the differences is difficult because each model folds in differ-

ent assumptions about, e.g., mass loss, convection and convective boundaries, and nuclear reaction networks, the differences can be qualitatively understood by the interaction between TDU and HBB in massive AGB stars (see discussion in § 2.2). Potentially give a little synopsis here in addition to the § 2.2 reference.

• The IMF-weighted C11+C15 yields are relatively independent of progenitor mass, while the other models considered here have more substantial yields from higher mass AGB stars. In all cases, the characteristic delay times for production are short compared to the SN Ia timescale (~few hundred Myr compared to ~1 Gyr). This result, however, likely does not extend to other elements produced in AGB stars (see discussion in § 4.2).

• For a smooth SFH, the gas phase [N/O]-[O/H] relation is relatively time-independent up to lookback times of ~6 - 8 Gyr in our fiducial model. Similar to arguments that have been made regarding the low-[α/Fe] population in the Milky Way (e.g. Schönrich & Binney 2009; Sharma et al. 2020; Johnson et al. 2021), we find that the [N/O]-[O/H] relation arises not out of an evolutionary sequence but as a superposition of endpoints of multiple evolutionary sequences. That is, the time evolution of each ring through the [N/O]-[O/H] plane is not the same line as the [N/O]-[O/H] relation that would be observed at the present day in our model Galaxy (see Fig. 6).

• Our models suggest that stellar migration has only a small impact on the N enrichment rate at a given radius and time because the characteristic delay-times of N production are significantly shorter than the migration timescale. In the case of Fe, the characteristic delay times are longer (~1 Gyr compared to a ~few hundred Myr), and based on this Johnson et al. (2021) find that the impact of migration on Fe enrichment rates is considerable (as much as a factor of ~3 in the SN Ia rate). The effect is sufficiently strong such that it may be enough to explain the intrinsically young sub-component of the young α-rich stars observed in the solar neighbourhood (Chiappini et al. 2015; Martig et al. 2015, 2016; Jofré et al. 2016; Yong et al. 2016; Izzard et al. 2018; Silva Aguirre et al. 2018; Warfield et al. 2021). Although our model suggests the impact may be larger when the Galaxy was young, this effect is only at the ≲ 0.05 dex level for N. This difference underscores the argument from Johnson et al. (2021) that in order for nucleosynthetic yields to migrate along with their progenitor stellar populations, the characteristic delay time for the production of some element must be comparable to the timescales of stellar migration.

• We are unable to reproduce the gas phase [N/O]-[O/H] relation as observed with any of the AGB star yield tables investigated here. The C11+C15 yields require an artificial amplification by a factor of ~3 in order to get the normalization correct, and we find similar results with the V13 yields (factor of ~2 amplification). The K10 yields predict [N/O] to decrease with increasing [O/H]: a slope with the wrong sign. Although the KL16+K18 yields predict a relatively flat [N/O]-[O/H] relation, they're able to explain the N abundances at low [O/H]; this is the only previously published yield model in this paper that is able to explain the N abundances at any metallicity without modification. Even with alternate forms for our CCSN yields as suggested by the non-rotating models of Woosley & Weaver (1995), Nomoto et al. (2013), Sukhbold et al. (2016), and Limongi & Chieffi (2018), our model is able to reproduce the observed [N/O]-[O/H] relation with neither the K10 nor the KL16+K18 yield models. There may be additional things to say on this if our investigation with a lowered O yield and a lowered η turns up something interesting. Fiorenzo was also able to do this with a differential wind.

• Our model successfully reproduces the correlations of [N/O] with [O/Fe] and stellar age when N abundances are corrected for internal mixing processes in stars. This is an important success of

the model, because Vincenzo et al. (2021) found that even after these corrections were made, the dichotomy in N abundances of thin- and thick-disc stars persisted. Vincenzo et al. (2021) also found the [N/O]-age relation in bins of [Fe/H] to be flat, whereas with uncorrected N abundances there is a significant negative slope. In agreement with Vincenzo et al. (2021), our model predicts the [N/O]-age relation to be flat when a selection in [Fe/H] is made. Both of these predictions trace back to our model predicting N abundances to increase in the ISM to correlate with the Fe abundance out to lookback times of ~10 Gyr; this correlation with Fe is significantly stronger than its correlation with O. Because of this, a range in [Fe/H] maps approximately to a range in [N/O], and [N/O] increases as [O/Fe] decreases, maintaining the chemical dichotomy between the two sequences. Even though this model is unsuccessful at reproducing the bimodality in [α/Fe] in detail (Johnson et al. 2021), a future version of the model which does will still predict such a dichotomy in N as well due to this correlation.

• We find that 25% sinusoidal oscillations in the SFR and SFE induce larger variability in the [N/O]-[O/H] relation than does stellar migration. Although this can be interpreted as higher/lower [N/O] at fixed [O/H], our models suggest that it's more accurate to characterize the scatter as a higher/lower [O/H] at fixed [N/O] (see discussion in § 4.4). With 25% variability in the SFE, we find that our model can accurately explain the intrinsic scatter in the gas phase [N/O]-[O/H] relation as inferred observationally by Schaefer et al. (2020). This supports their conjectures that there is a causal relationship behind this correlation and that radial migration is not a significant contributing factor to the scatter in their data. Although real galaxies likely have variations in their SFR or SFE that are neither perfectly sinusoidal nor with a constant amplitude, such effects induce variations in the [N/O]-[O/H] plane which, in a sufficiently large sample, would present observationally as intrinsic scatter. Our models suggest that typical variations in these quantities cause variability in the relation which is considerably larger than that caused by stellar migration.

• The results outlined in this paper highlight the importance of empirically calibrated yields of all elements from all nucleosynthetic sources in GCE models. The combination of theoretically predicted yields with flexible computational tools such as VICE can provide powerful constraints for future models of stellar evolution and element production.

REFERENCES

Adams S. M., Kochanek C. S., Gerke J. R., Stanek K. Z., Dai X., 2017, MNRAS, 468, 4968

Andrews B. H., Weinberg D. H., Schönrich R., Johnson J. A., 2017, ApJ, 835, 224

Asplund M., Grevesse N., Sauval A. J., Scott P., 2009, ARA&A, 47, 481

Basinger C. M., Kochanek C. S., Adams S. M., Dai X., Stanek K. Z., 2021, MNRAS, 508, 1156

Belfiore F., et al., 2017, MNRAS, 469, 151

Berg D. A., et al., 2012, ApJ, 754, 98

Berg D. A., Pogge R. W., Skillman E. D., Croxall K. V., Moustakas J., Rogers N. S. J., Sun J., 2020, ApJ, 893, 96

Bigiel F., Leroy A., Walter F., Blitz L., Brinks E., de Blok W. J. G., Madore B., 2010, AJ, 140, 1194

Bilitewski T., Schönrich R., 2012, MNRAS, 426, 2266

Bird J. C., Kazantzidis S., Weinberg D. H., 2012, MNRAS, 420, 913

Bird J. C., Kazantzidis S., Weinberg D. H., Guedes J., Callegari S., Mayer L., Madau P., 2013, ApJ, 773, 43

Bird J. C., Loebman S. R., Weinberg D. H., Brooks A. M., Quinn T. R., Christensen C. R., 2021, MNRAS, 503, 1815

Bland-Hawthorn J., Gerhard O., 2016, ARA&A, 54, 529

Bloecker T., 1995, A&A, 297, 727

Bovy J., Leung H. W., Hunt J. A. S., Mackereth J. T., García-Hernández D. A., Roman-Lopes A., 2019, MNRAS, 490, 4740

Brooks A. M., Zolotov A., 2014, ApJ, 786, 87

Brooks A. M., Papastergis E., Christensen C. R., Governato F., Stilp A., Quinn T. R., Wadsley J., 2017, ApJ, 850, 97

Bundy K., et al., 2015, ApJ, 798, 7

Chiappini C., et al., 2015, A&A, 576, L12

Chieffi A., Limongi M., 2004, ApJ, 608, 405

Chieffi A., Limongi M., 2013, ApJ, 764, 21

Christensen C., Quinn T., Governato F., Stilp A., Shen S., Wadsley J., 2012, MNRAS, 425, 3058

Christensen C. R., Brooks A. M., Fisher D. B., Governato F., McCleary J., Quinn T. R., Shen S., Wadsley J., 2014a, MNRAS, 440, L51

Christensen C. R., Governato F., Quinn T., Brooks A. M., Shen S., McCleary J., Fisher D. B., Wadsley J., 2014b, MNRAS, 440, 2843

Christensen C. R., Davé R., Governato F., Pontzen A., Brooks A., Munshi F., Quinn T., Wadsley J., 2016, ApJ, 824, 57

Cristallo S., et al., 2011, ApJS, 197, 17

Cristallo S., Straniero O., Piersanti L., Gobrecht D., 2015, ApJS, 219, 40

de los Reyes M. A. C., Kennicutt Robert C. J., 2019, ApJ, 872, 16

Dopita M. A., Kewley L. J., Sutherland R. S., Nicholls D. C., 2016, Ap&SS, 361, 61

Ellison S. L., Lin L., Thorp M. D., Pan H.-A., Scudder J. M., Sánchez S. F., Bluck A. F. L., Maiolino R., 2021, MNRAS, 501, 4777

Ertl T., Janka H. T., Woosley S. E., Sukhbold T., Ugliano M., 2016, ApJ, 818, 124

Frankel N., Rix H.-W., Ting Y.-S., Ness M., Hogg D. W., 2018, ApJ, 865, 96

Frankel N., Sanders J., Rix H.-W., Ting Y.-S., Ness M., 2019, ApJ, 884, 99

Frischknecht U., et al., 2016, MNRAS, 456, 1803

Gerke J. R., Kochanek C. S., Stanek K. Z., 2015, MNRAS, 450, 3289

Gilroy K. K., 1989, ApJ, 347, 835

Governato F., et al., 2012, MNRAS, 422, 1231

Griffith E. J., Sukhbold T., Weinberg D. H., Johnson J. A., Johnson J. W., Vincenzo F., 2021, arXiv e-prints, p. arXiv:2103.09837

Grisoni V., Matteucci F., Romano D., 2021, arXiv e-prints, p. arXiv:2109.03642

Gronow S., Cote B., Lach F., Seitenzahl I. R., Collins C. E., Sim S. A., Roepke F. K., 2021a, arXiv e-prints, p. arXiv:2103.14050

Gronow S., Collins C. E., Sim S. A., Röpke F. K., 2021b, A&A, 649, A155

Heger A., Woosley S. E., 2010, ApJ, 724, 341

Henry R. B. C., Edmunds M. G., Köppen J., 2000, ApJ, 541, 660

Hurley J. R., Pols O. R., Tout C. A., 2000, MNRAS, 315, 543

Izotov Y. I., Thuan T. X., Guseva N. G., 2012, A&A, 546, A122

Izzard R. G., Preece H., Jofre P., Halabi G. M., Masseron T., Tout C. A., 2018, MNRAS, 473, 2984

James B. L., Koposov S., Stark D. P., Belokurov V., Pettini M., Olszewski E. W., 2015, MNRAS, 448, 2687

Jenkins A., 1992, MNRAS, 257, 620

Jenkins A., Binney J., 1990, MNRAS, 245, 305

Jofré P., et al., 2016, A&A, 595, A60

Johnson J. A., 2019, Science, 363, 474

Johnson J. W., Weinberg D. H., 2020, MNRAS, 498, 1364

Johnson J. W., et al., 2021, arXiv e-prints, p. arXiv:2103.09838

Karakas A. I., 2010, MNRAS, 403, 1413

Karakas A. I., Lugaro M., 2016, ApJ, 825, 26

Karakas A. I., Lugaro M., Carlos M., Cseh B., Kamath D., García-Hernández D. A., 2018, MNRAS, 477, 421

Kennicutt Robert C. J., 1998, ApJ, 498, 541

Kennicutt R. C., Evans N. J., 2012, ARA&A, 50, 531

Kennicutt Robert C. J., de los Reyes M. A. C., 2021, ApJ, 908, 61

Kodama T., Arimoto N., 1997, A&A, 320, 41

Korn A. J., Grundahl F., Richard O., Mashonkina L., Barklem P. S., Collet R., Gustafsson B., Piskunov N., 2007, ApJ, 671, 402

Kroupa P., 2001, MNRAS, 322, 231

Krumholz M. R., Burkhart B., Forbes J. C., Crocker R. M., 2018, MNRAS, 477, 2716

Lacey C. G., Fall S. M., 1985, ApJ, 290, 154

Lagarde N., Decressin T., Charbonnel C., Eggenberger P., Ekström S., Palacios A., 2012, A&A, 543, A108

Larson R. B., 1974, MNRAS, 166, 585

Leroy A. K., Walter F., Brinks E., Bigiel F., de Blok W. J. G., Madore B., Thornley M. D., 2008, AJ, 136, 2782

Leroy A. K., et al., 2013, AJ, 146, 19

Licquia T. C., Newman J. A., 2015, ApJ, 806, 96

Limongi M., Chieffi A., 2006, ApJ, 647, 483

Limongi M., Chieffi A., 2018, ApJS, 237, 13

Lind K., Korn A. J., Barklem P. S., Grundahl F., 2008, A&A, 490, 777

Liu L., Gao Y., Greve T. R., 2015, ApJ, 805, 31

Maeder A., Meynet G., 1989, A&A, 210, 155

Maeder A., Zahn J.-P., 1998, A&A, 334, 1000

Majewski S. R., et al., 2017, AJ, 154, 94

Marigo P., 2002, A&A, 387, 507

Martig M., et al., 2015, MNRAS, 451, 2230

Martig M., et al., 2016, MNRAS, 456, 3655

Matteucci F., Francois P., 1989, MNRAS, 239, 885

Miglio A., et al., 2021, A&A, 645, A85

Mihalas D., Binney J., 1981, Galactic astronomy. Structure and kinematics

Minchev I., Famaey B., Combes F., Di Matteo P., Mouhcine M., Wozniak H., 2011, A&A, 527, A147

Minchev I., Chiappini C., Martig M., 2013, A&A, 558, A9

Minchev I., Chiappini C., Martig M., 2014, A&A, 572, A92

Minchev I., Steinmetz M., Chiappini C., Martig M., Anders F., Matijevic G., de Jong R. S., 2017, ApJ, 834, 27

Mollá M., Vílchez J. M., Gavilán M., Díaz A. I., 2006, MNRAS, 372, 1069

Munshi F., et al., 2013, ApJ, 766, 56

Nomoto K., Kobayashi C., Tominaga N., 2013, ARA&A, 51, 457

Padovani P., Matteucci F., 1993, ApJ, 416, 26

Paxton B., Bildsten L., Dotter A., Herwig F., Lesaffre P., Timmes F., 2011, ApJS, 192, 3

Paxton B., et al., 2013, ApJS, 208, 4

Paxton B., et al., 2015, ApJS, 220, 15

Paxton B., et al., 2018, ApJS, 234, 34

Pejcha O., Thompson T. A., 2015, ApJ, 801, 90

Pilyugin L. S., Vílchez J. M., Thuan T. X., 2010, ApJ, 720, 1738

Rogers N. S. J., Skillman E. D., Pogge R. W., Berg D. A., Moustakas J., Croxall K. V., Sun J., 2021, ApJ, 915, 21

Sánchez S. F., 2020, ARA&A, 58, 99

Schaefer A. L., Tremonti C., Belfiore F., Pace Z., Bershady M. A., Andrews B. H., Drory N., 2020, ApJ, 890, L3

Schönrich R., Binney J., 2009, MNRAS, 396, 203

Sellwood J. A., Binney J. J., 2002, MNRAS, 336, 785

Sharma S., Hayden M. R., Bland-Hawthorn J., 2020, arXiv e-prints, p. arXiv:2005.03646

Silva Aguirre V., et al., 2018, MNRAS, 475, 5487

Skillman E. D., Berg D. A., Pogge R. W., Moustakas J., Rogers N. S. J., Croxall K. V., 2020, ApJ, 894, 138

Souto D., et al., 2018, ApJ, 857, 14

Souto D., et al., 2019, ApJ, 874, 97

Sukhbold T., Ertl T., Woosley S. E., Brown J. M., Janka H. T., 2016, ApJ, 821, 38

Suliga A. M., Shalgar S., Fuller G. M., 2020, arXiv e-prints, p. arXiv:2012.11620

Tacconi L. J., et al., 2018, ApJ, 853, 179

Vassiliadis E., Wood P. R., 1993, ApJ, 413, 641

Ventura P., Di Criscienzo M., Carini R., D'Antona F., 2013, MNRAS, 431, 3642

Ventura P., di Criscienzo M., D'Antona F., Vesperini E., Tailo M., Dell'Agli F., D'Ercole A., 2014, MNRAS, 437, 3274

Ventura P., Karakas A., Dell'Agli F., García-Hernández D. A., Guzman-Ramirez L., 2018, MNRAS, 475, 2282

Ventura P., Dell'Agli F., Lugaro M., Romano D., Tailo M., Yagüe A., 2020, A&A, 641, A103

Vincenzo F., Kobayashi C., 2020, MNRAS, 496, 80

Vincenzo F., Belfiore F., Maiolino R., Matteucci F., Ventura P., 2016a, MN-RAS, 458, 3466

Vincenzo F., Matteucci F., de Boer T. J. L., Cignoni M., Tosi M., 2016b, MNRAS, 460, 2238

Vincenzo F., et al., 2021, arXiv e-prints, p. arXiv:2106.03912

Wadsley J. W., Stadel J., Quinn T., 2004, New Astron., 9, 137

Warfield J. T., et al., 2021, AJ, 161, 100

Weinberg D. H., Andrews B. H., Freudenburg J., 2017, ApJ, 837, 183

Weinberg D. H., et al., 2019, ApJ, 874, 102

Weinberg D. H., et al., 2021, arXiv e-prints, p. arXiv:2108.08860

Woosley S. E., Weaver T. A., 1995, ApJS, 101, 181

Yong D., et al., 2016, MNRAS, 459, 487

Zahn J. P., 1992, A&A, 265, 115

Zolotov A., et al., 2012, ApJ, 761, 71

Appendices

A VICE

VICE[1] is an open-source PYTHON package designed to model chemical enrichment processes in galaxies with a generic, flexible model. With this paper, we mark the release of version 1.3.0 which presents a handful of new features:

   (i) Users may select a mass-lifetime relation for stars from a list of several parameterized forms taken from the literature. Previously, only a single power-law was implemented; now, the options include the equations presented in:

- Vincenzo et al. (2016b)
- Hurley, Pols & Tout (2000)
- Kodama & Arimoto (1997)
- Padovani & Matteucci (1993)
- Maeder & Meynet (1989)
- Larson (1974) (default)

   (ii) We have added two additional tables of AGB star yields sampled at various progenitor masses and metallicities: the KL16+K18 and V13 models presented in this paper are new to VICE (see discussion in § 2.2 for details).

   (iii) We have built in the SN Ia yields presented in Gronow et al. (2021b,a). These tables present yields for double detonations of sub-Chandrasekhar mass carbon-oxygen white dwarfs at various progenitor metallicities.

Although VICE includes built in SN and AGB star yield tables, users are not required to adopt any one of them for use in their chemical evolution models. Instead, it allows arbitrary functions of metallicity for both CCSN and SN Ia yields and functions of progenitor mass and metallicity for AGB star yields. It provides similar flexibility for additional parameters typically built into GCE models. VICE's backend is implemented entirely in ANSI/ISO C, providing it with the powerful computing speeds of a compiled library while retaining such scientific flexibility within the easy-to-use framework of PYTHON.

   VICE supports Mac and Linux operating systems; Windows users should install and use VICE entirely within the Windows Subsystem for Linux. On machines with x86_64 hardware, it can be installed in a terminal via `pip install vice`. Users running ARM64 hardware (e.g. the new Apple Silicon computers) must install VICE by compiling from source, instructions for which can be found in the documentation. After installing, running `vice --docs` and `vice --tutorial` from a `Unix` terminal will launch a web browser to the documentation and to a jupyter notebook intended to familiarize first time users with VICE's API.

---

[1] Install (PyPI): https://pypi.org/project/vice
Documentation: https://vice-astro.readthedocs.io
Source Code: https://github.com/giganano/VICE.git